Tectonic controls on Ni and Cu contents of primary mantle-derived magmas for the formation of magmatic sulfide deposits

Revision 2

Zhuosen Yao[a,b,d], Kezhang Qin[a,b,c*], James E. Mungall[d]

[a] Key Laboratory of Mineral Resources, Institute of Geology and Geophysics, Chinese Academy of Sciences, Beijing, 100029, China

[b] University of Chinese Academy of Sciences, Beijing 100049, China

[c] CAS Center for Excellence in Tibetan Plateau Earth Science, Beijing 100101, China

[d] Department of Earth Sciences, Carleton University, 1125 Colonel By Drive, Ottawa, ON K1S 5B6, Canada

* Corresponding author. E-mail address: kzq@mail.iggcas.ac.cn

Abstract

We have modeled the genesis of primary mantle-derived magma to explore the controls exerted on its Ni-Cu ore potential by water content, pressure and mantle potential temperature (T_p). During decompression melting, Ni concentration in primary magma decreases with increasing degree of melting, in contradiction to long-held understanding obtained from previous isobaric melting models. Pressure exerts a first-order control on the ore potential of primary plume-derived melt, such that plumes rising beneath thick lithosphere with melting paths terminating at relatively high pressure generate Ni-rich melts. Additionally, as plumes with higher T_p produce more Ni-rich melt at a higher pressure, the magmatism related to hotter plume-centers may have the greatest ore potential. On the other hand, the strong dependence of Cu behavior upon the presence or absence of residual sulfide is partly countered in decompression melting. Significant influences of mantle-contained water on Ni and Cu partitioning are restricted to low-degree melting. While release of H_2O in lithosphere delamination may trigger voluminous magmatism, the Ni concentration in melt is far lower than in melt generated from plumes. Furthermore, if isobaric melting dominates when the subcontinental lithospheric mantle (SCLM) is heated by underlying hotter plumes, the plume-lithosphere interaction plays no active role in the Ni ore potential of primary magma because derived melt volumes are relatively small. In subduction zones, flux-melting of the mantle wedge tends to generate cool Ni-poor melts, however hot subduction zones may produce magmas with increased metal concentrations. Overall, the anticipated ranges of Ni contents in primary melts are strongly controlled by tectonic setting, with range of 100-300 ppm in subduction zones, 230-450 ppm in mid-ocean ridges, and 500-1300 ppm in plume suites. There are only minor differences in the Cu concentrations of primitive magmas generated from diverse tectonic settings, despite the variations in Cu partitioning behaviors.

Keywords mantle partial melting, Ni and Cu partitioning behaviors, tectonic settings, ore potential of primary magma, forward model

1. Introduction

Magmatic Ni-Cu-(PGE) sulfide deposits, hosting ~56 % and >96 % respectively of global resources of Ni and PGEs, are formed as the result of segregation and accumulation of immiscible sulfide liquids from mafic and/or ultramafic mantle-derived magmas (Arndt et al. 2005; Barnes and Lightfoot 2005; Naldrett 2010, 2011; Mungall 2014; Barnes et al. 2016; Barnes and Robertson 2018). The characteristics of primary magma that promote the formation of magmatic Ni-Cu-(PGE) deposits in various tectonic settings still remain poorly constrained (Arndt et al. 2005; Zhang et al. 2008) despite the general consensus that picritic and komatiitic magmas are best. Although the existence of an unusually metal-rich primary melt has not been widely considered as a necessity for the formation of most magmatic Ni-Cu-(PGE) deposits, it is also evident that relatively metal-poor magmas would not be optimal. Petrological information regarding primary magma composition that can be obtained from intrusive samples is not straightforward as primary magmas are likely to be modified by partial crystallization, assimilation, and mixing in crustal environments (Herzberg and Asimow 2015).

The use of forward models to compute the geochemistry of melts and partitioning behaviors of Ni, Cu and PGEs during partial melting offers us a distinctive angle to explore the ore potential of primary magma. Naldrett (2010, 2011) modeled the partitioning behaviors of Ni, Cu, Pt and Pd in the isobaric melting of mantle, an approach followed in several more recent studies (e.g., Li et al. 2012; Lightfoot et al. 2012; Jowitt and Ernst 2013; Mao et al. 2014). Lee et al. (2012) quantified the evolution of Cu concentrations in mantle-derived melts by modeling fractional melting of a fertile mantle at fixed proportions of mineral phases and P-T condition, advocating Cu content can be used to trace the presence of sulfide in the source (Liu et al. 2014; Le Roux et al. 2015). More recently, polybaric melting models were developed to predict the concentrations of PGE in primary melt and the corresponding restites (Mungall and Brenan 2014; Aulbach et al. 2016), as well as the sulfur budget in MORBs (Ding and Dasgupta 2017). The compositions of primary melts can be controlled by: 1) the composition and thermal state of mantle source; 2) the type of melting (e.g., fractional, equilibrium or continuous melting); 3) melting conditions, including the temperature, pressure, and volatile components (Asimow et al. 2001; Herzberg and O’Hara 2002; Asimow and Langmuir 2003; Arndt et al. 2005; Herzberg and Asimow 2015). These factors, which dominate the extent and output of partial melting, are highly variable in different tectonic settings, e.g., mid-ocean ridges, mantle plumes and subduction zones. Consequently, the geochemical characteristics and ore potentials of primary magmas involved in magmatic deposits must bear a close relationship to geodynamic environments. Existing models have not considered all of these parameters together to provide a detailed and realistic picture of this complex process in the broad range of tectonic settings in which mantle melting occurs.

In this contribution, we present a comprehensive model optimized for mantle melting in the pressure range of 0-4 GPa, using the alphaMELTS thermodynamic software (Ghiorso and Sack 1995; Ghiorso et al. 2002; Asimow et al. 2004; Smith and Asimow 2005) to constrain phase equilibria, in conjunction with recent refinements of partition coefficients to trace the behaviors of Ni and Cu during the partial melting of mantle in various tectonic settings as realistically as possible with the current state of knowledge.

2. Model descriptions

Approaches to modeling mantle melting can be achieved via empirical parameterizations (Katz et al. 2003; Till et al. 2012; Kimura and Kawabata 2014; Mungall and Brenan 2014) and thermodynamic models (Ghiorso et al. 2002; Ueki and Iwamori 2013; Jennings and Holland 2015), each with their own advantages and weaknesses (Supplementary 1). pMELTS is a popular model to track the phase relations and compositional variations for partial melting systems as it can be applied to various melting mechanisms (e.g., fractional, continuous or equilibrium) and P-T conditions (e.g., isobaric, polybaric or dynamic P-T paths) (Ghiorso et al. 2002) that cannot be addressed quantitatively with purely empirical models. Although the topology and phase proportions in mantle melting reactions are captured well by alphaMELTS, it reproduces experimental temperature and MgO content of melt at a given melt fraction in due to the overstabilization of clinopyroxene, and gives relative large disparities at high pressure exceeding 4 GPa (Ghiorso et al. 2002; Ueki and Iwamori 2013; Kimura and Kawabata 2014; Jennings and Holland 2015). Here, we have adopted the latest version of alphaMELTS, which includes pMELTS having updated garnet and spinel models and offers an improved match to experimental data (Supplementary 1), but caution is still warranted in the entire calculation. Below we summarize the controls on partitioning behaviors of Ni and Cu during partial melting exerted by a range of parameters, including pressure, temperature, oxygen fugacity, source composition, H_2O concentration, and the partition coefficients between silicate melt, minerals and sulfide liquid.

2.1 Source compositions

Concentrations of major elements (including Ni) of primitive source from McDonough and Sun (1995), were used to model the partial melting of primitive mantle (PM, Table 1). Cu concentration in PM was assumed to be 24 ppm (Wang and Becker 2015), within the estimated range of 20-30 ppm (Sun 1982; O'Neill 1991;

McDonough and Sun 1995; Lorand and Luguet 2016; Barnes et al. 2016). For the melting models of the MORB mantle source, we used the depleted MORB mantle (DMM) (Workman and Hart 2005). Compared to the primitive mantle, DMM has been depleted by 2-3% ancient melt extraction. The Ni abundance in DMM is 1886 ppm, but the Cu concentration was not mentioned by Workman and Hart (2005). Because the presence of residual sulfide phase at such low degree of melt extraction would minimize depletion of Cu, we assume that DMM has the same concentration of Cu as PM (Table 1).

The composition of the sub-continental lithospheric mantle (SCLM) has a broad range, and is related to the age of overlying crust (Griffin et al. 1998, 2009). We used three estimates of SCLM composition based on the Griffin et al. (1999) classification, wherein A-SCLM occurs in areas where the crust has been unaffected since ≥ 2.5 Ga; P-SCLM has been formed or modified in the range of 2.5-1.0 Ga; and T-SCLM experienced tectonism and melting ≤ 1.0 Ga (Table 1). The Ni amounts in A-, T- and P-SCLM are 2357 ppm, 2200 ppm and 2043 ppm, respectively (Griffin et al. 2009). Additionally, the Cu concentrations of most massif and xenolith peridotites exhibit a positive correlation with Al_2O_3 content, an indicator of the fertility (or melt depletion) of peridotites (Wang and Becker 2015). Based on the Al_2O_3 contents from the A-, T- and P-SCLM compositions (Griffin et al. 2009), in conjunction with the values of Al_2O_3/Cu from DMM, the Cu concentrations in A-, T- and P-SCLMs were taken to be 1.8, 11.5 and 21.1 ppm, respectively.

The mantle wedge above subduction zones is a complex environment where subducted inputs are mixed with the convecting mantle to generate magmas (Stern 2002), and hence, its partial melting is a multi-stage and multi-source process (Cole et al. 1990). The composition of mantle wedge may be highly variable from one location to another. We use Workman and Hart's (2005) DMM to approximate the composition of the sub-arc mantle to facilitate comparison of partitioning behaviors of Ni and Cu between the mantle wedges and mid-ocean ridges. The restites resulting after 5%, 10%, 15% and 20% melt extraction from the isobaric melting of DMM at 1 GPa were considered as the plausible approximations of initial source compositions within the mantle wedge. The transfer of ore-forming metals from slab-derived inputs into mantle wedge is restricted (e.g., Mungall 2002; Jenner et al. 2010; Lee et al. 2012), and hence, the source was assumed to contain 24 ppm Cu.

2.2 Water content

There is a growing database on the water content in nominally anhydrous minerals from a wide range of mantle-derived rocks (Peslier 2010). Although previous estimates of H_2O content of the MORB source vary from 100 to 340 ppm (Bell and Rossman 1992; Bolfan-Casanova 2005), the most recent estimates range from 50 to 200 ppm (Peslier 2010, and references therein). A range of 0-250 ppm H_2O was adopted in our model.

The source of the oceanic island basalts (OIBs), which is a common component of mantle plume material (Wilson 1963; White 2010), appears to be more hydrous than MORB-source mantle (200-550 ppm H_2O; Bell and Rossman 1992 or 450-700 ppm H_2O; Bolfan-Casanova 2005). Based on the H_2O analyses of glasses and melt inclusions, the sources of OIBs are richer in water than DMM, containing 300-1000 ppm H_2O (Hirschmann 2006; Peslier 2010). Comparably, the H_2O contents of basaltic glasses from the Ontong Java and Kerguelen oceanic plateaus (~4000-6900 ppm) are also higher than that of MORBs (~2500 ppm) (Michael 2000; Wallace 2002). More recently, the estimated H_2O contents of the mantle sources for Siberian Traps, Karoo LIP, Tarim LIP, Emeishan LIP, Yellowstone hotspot track and Caribbean LIP are from 750 to ~6000 ppm (Liu et al. 2017). Additionally, H_2O may have been transferred from a hypothesized water-rich transition zone to Archaean plumes, producing hydrous komatiites with ~0.6 wt. % water (Sobolev et al. 2016). Therefore, the H_2O in mantle plumes has a broad range (0-6000 ppm in this modeling), and its source should have one or more H_2O-rich reservoirs that feed plume-related magmatism (Hirschmann 2006).

The recalculated water contents of whole-rock peridotite xenoliths from continental cratons are somewhat lower than the MORB source, e.g., Kaapvaal craton (16-175 ppm H_2O, average of 82 ppm) (Bell and Rossman 1992; Peslier et al. 2012). Although the whole-rock H_2O content of SCLM can be affected by many complex processes, e.g., metasomatism (Siberia craton, 38-293 ppm, Doucet et al. 2014; Ragozin et al. 2014), lithospheric thinning (North China craton, mostly <50 ppm, Yang et al. 2008; Xia et al. 2010) and plume-lithosphere interaction (Tranzanian craton, 7-48 ppm, Hui et al. 2015), with few exceptions it stays in a relatively low range, ~0-150 ppm.

As slab-derived fluids and melts have a broad range of compositions, the H_2O content of the mantle wedge may be highly variable from one location to another, with a reported range from 250 to >2500 ppm (Peslier et al. 2002; Dixon et al. 2004; Peslier and Luhr 2006; Peslier 2010).

2.3 Mantle potential temperature

Mantle potential temperature (T_p) represents the hypothetical temperature that mantle would have if it was adiabatically decompressed to surface without melting (Fig. 1) (McKenzie and Bickle 1988). The ranges of T_p in different tectonic environments mostly do not overlap (Lee et al. 2009), so the inferences of T_p based on basaltic magma compositions can be used to constrain the tectonic setting of basaltic magmatic suites (Putirka 2005; Herzberg et al. 2007; Herzberg and Asimow 2008).

Based on the global database of basaltic magmatism, Lee et al. (2009) depicted the Earth's thermal state (T_p) and magmatism in various geologic environments. MORB compositions from the Mid-Atlantic Ridge and the East Pacific Rise showed that the T_p of their mantle is near 1350-1400°C (Lee et al. 2009), which is hotter than previous estimates (McKenzie and Bickle 1988), but falls within the range of recent estimations for mid-ocean ridges (1280-1400ºC by Herzberg et al. 2007 and 1300-1570ºC by Langmuir et al. 1993), considering that the aggregated error on T_p may be as large as ±77ºC due to uncertainties in estimates of melting fraction and mantle olivine composition (Putirka 2016).

Furthermore, numerous petrological studies of basalts from large igneous provinces (LIPs) and ocean islands infer higher T_p than the oceanic ridges, which strongly supports the mantle plume model (Thompson and Gibson 2000; Putirka 2005, 2016; Putirka et al. 2007; Herzberg et al. 2007; Lee et al. 2009; Herzberg and Gazel 2009). The estimated range of T_p for plume-related magmatism is large, even for an individual mantle plume occurrence (Herzberg and Asimow 2008; Herzberg and Gazel 2009). The T_p of Hawaii and Iceland reach as high as 1722ºC and 1616ºC, respectively (Putirka et al. 2007; Herzberg and Asimow 2008, 2015). More broadly, almost all of the data from plume-related basalts point to a T_p of more than 1500ºC, and the T_p anomaly required to merit the term "plume" can be set to be 220-320 ºC higher than the ambient mantle (Putirka 2016).

2.4 Choice of Partition Coefficients between minerals and melt

Ni is compatible in olivine, which is the most abundant mineral in the Earth's upper mantle. As a result, the behavior of Ni is mostly determined by its distribution between olivine and silicate melt as defined by its Nernst partition coefficient ($D_{Ni}^{Ol/melt}$). We used a parameterized equation of $D_{Ni}^{Ol/melt}$ that accounts for the effects of temperature and melt composition (Matzen et al. 2017a). Ni is also compatible in orthopyroxene. Experiments by Laubier et al. (2014) under anhydrous and oxidized conditions at 0.1 MPa and 1155-1180°C indicated that the partition coefficient $D_{Ni}^{Opx/melt}$ was 7.38±2.56, whereas high pressure (1.5-2 GPa), high temperature (1300-1500 °C) and relatively reducing conditions may result in a low $D_{Ni}^{Opx/melt}$ (3.69-4.38; Le Roux et al. 2011). Here, we followed the model of Beattie et al. (1991), which gives $D_{Ni}^{Opx/melt}$ as a function of the mole fractions of MgO in the melt and orthopyroxene. Although this is a temperature-, pressure-independent model, we think the influences of temperature and pressure can be reflected in the variations of MgO in melt, and the equation of Beattie et al. (1991) also provides a good description of experimental data for the Ni partitioning between olivine and melt (Herzberg et al. 2013), lending confidence to the orthopyroxene model. The $D_{Ni}^{Cpx/melt}$ was calculated as a function of temperature, pressure and $D_{Ni}^{Opx/melt}$ (Seitz et al. 1999), whereas the parameterization of $D_{Ni}^{Grt/melt}$ is based on the experimental measurements of partitioning of Ni between olivine and garnet (Canil 1999).

In contrast to Ni, as constrained by several recent studies, Cu is a mildly incompatible element in the major mineral phases of mantle (Fellows and Canil 2012; Lee et al. 2012; Liu et al. 2014; Le Roux et al. 2015). The measured $D_{Cu}^{minerals/melt}$ from groundmass and phenocrysts pairs in natural samples (Lee et al. 2012) are usually equivalent to or lower than the values obtained from experiments (Fellows and Canil 2012; Liu et al. 2014; Le Roux et al. 2015). In addition, Liu et al. (2014) found that increasing fO_2 (>ΔFMQ+1.2) would result in the increase of $D_{Cu}^{mineral/melt}$ for olivine, orthopyroxene, spinel and possible clinopyroxene, presumably due to increasing Cu^{2+}/Cu^{+} in the system. In this regard, we adopted the absolute upper values for high-pressure Cu partitioning ($D_{Cu}^{Ol/melt}$, 0.13; $D_{Cu}^{Opx/melt}$, 0.12; $D_{Cu}^{Cpx/melt}$, 0.09; $D_{Cu}^{Grt/melt}$, 0.042; $D_{Cu}^{Spl/melt}$, 0.25) based on the recent work of Le Roux et al. (2015).

2.5 Influence of sulfide within source

Fe-Ni-Cu base metal sulfides (BMSs) have been widely observed as intergranular grains and as inclusions within silicate minerals from a variety of peridotites and xenoliths (Harvey et al. 2016 and references therein). The partition coefficients between sulfide and melt are large for Cu (~290-390 for komatiite, 360-460 for basalt, and 420-560 for andesite, Kiseeva et al. 2017), with the result that the bulk partitioning of Cu during partial melting strongly depends on how sulfide mode varies during melt extraction.

Although the canonical S content of primitive mantle is ~250 ppm (McDonough and Sun 1995; Lorand and Luguet 2016 and references therein), the bulk S abundance of DMM is closer to 150-200 ppm (Lorand and Luguet 2016), which coincides with the estimated value in recent models (e.g., 100-200 ppm in Ding and Dasgupta 2017; 195±45 ppm from Nielsen et al. 2014; 185 ppm in Mungall and Brenan 2014; 165 ppm from Shimizu et al. 2016). The S contents of A-, P- and T-SCLM (Table 1) were assumed following the linear decrease in sulfur content with decreasing Al_2O_3 (Wang and Becker 2013), although this simple relationship could be affected by addition or removal of S by S-unsaturated fluids or melts. In the mantle wedge above subduction zones, the estimated S contents range from 250 to 500 ppm (Métrich et al. 1999; De Hoog et al. 2001), which may be triggered by addition of excess S in the slab-derived fluids (Mungall 2002; Jégo and Dasgupta 2013, 2014).

Sulfur in solid mantle materials is hosted by sulfide phases which dissolve progressively during partial melting of mantle. The S content in melt at equilibrium with sulfide liquid (SCSS) is influenced by pressure, temperature, melt composition (including water content), oxygen fugacity and the sulfide composition (Mavrogenes and O'Neill 1999; Liu et al. 2007; Moretti and Baker 2008; Li and Ripley 2009; Ariskin et al. 2013; Fortin et al. 2015; Lesne et al. 2015; Smythe et al. 2017). At the relative low oxygen fugacity that obtains during partial melting of DMM, PM and SCLM (Foley 2010; Cottrell and Kelley 2011), effectively all S within melt remains in the S^{2-} redox state. The f_{O_2} of mantle wedge above subducting slabs is widely considered to be relatively oxidized due to the addition of subduction-released oxidized fluids and/or melts (Mungall 2002; Kelley and Cottrell 2009; Richards 2015), and the island arcs (average ΔFMQ+1.3) are more oxidized than continental arcs (average ΔFMQ-0.16) (Foley 2010). At high oxygen fugacity (log f_{O_2} > ΔFMQ+1), the dominant speciation of S in melt changes from S^{2-} to S^{6+}, and the total S solubility increases dramatically (Jugo et al. 2010). We have adopted the SCSS model of Fortin et al. (2015) for the MORB generation and the sub-arc mantle wedge melting due to its success at the corresponding pressure-temperature conditions (Ding and Dasgupta 2017). But for higher pressure melting (PM and SCLM), we used the new model of Smythe et al. (2017) that incorporates the influences of sulfide composition and extends the pressure and temperature ranges of SCSS. The differences between modeling outputs that would result from the use of various SCSS models are discussed in the Supplementary 2.

We have adopted a recent thermodynamic model that accounts for the effects of temperature and sulfide composition on the partitioning of Ni and Cu between sulfide liquids and anhydrous silicate melt at 1.5 GPa and 1300-1700ºC (Kiseeva and Wood 2013, 2015) in lieu of previous assumptions of fixed values (e.g., Lee et al. 2012; Naldrett 2010, 2011; Ding and Dasgupta 2017).

3. Mechanism of partial melting in mantle

3.1 Polybaric continuous melting of DMM beneath Mid-Ocean Ridges

Models for the production of MORB have been based on empirical or thermodynamic parameterization (McKenzie and Bickle 1988; Langmuir et al. 1993; Asimow et al. 2001; Niu and O'Hara 2008). We use the polybaric continuous melting model via the alphaMELTS, which derives plausible results for MORB compositions, crustal thickness and axial depth of global Mid-Ocean Ridges (Asimow et al. 2001; Asimow and Langmuir 2003; Asimow 2004).

In a continuous melting model, a fixed volume (or mass) proportion of melt is retained in residual mantle after extraction, defining an intermediate state between fractional and batch melting. The approach for computing the polybaric continuous melting of mantle was described by Asimow et al. (2001). Melting is simulated by the decompression process from the solidus to surface in 10 MPa steps. Once the melt fraction by volume exceeds a fixed threshold, the extra melt in each increment is extracted, and the composition and entropy of the residual system are used as reference for the next increment. Increments of extracted liquid are integrated as the pooled magmatic output of mantle melting beneath the mid-ocean ridges. We compared results using a triangular melting prism (e.g., Mungall and Brenan 2014) and the simpler vertical column (e.g., passive flow model of Asimow et al. 2001) and found little difference for Cu and Ni. The results presented here are for a simple vertical melting column. The influence of water on melting behavior was taken into account throughout this entire calculation by simulating the equilibrium distribution of hydrogen among silicate melts and nominally anhydrous minerals (Asimow et al. 2004; Asimow 2004). The measurements of global $Fe^{3+}/\sum Fe$ ratios of MORB glasses provided an accurate approximation for the oxygen fugacity of the MORB source, which is distributed around the fayalite-magnetite-quartz (FMQ) buffer (~ΔFMQ+0.07 by Cottrell and Kelley 2011; ΔFMQ+0.1 by Berry et al. 2018; or ΔFMQ-0.18 by Zhang et al. 2018). The modeling results of DMM melting under different fixed oxygen fugacity (from ΔFMQ-1.0 to ΔFMQ+0.6) show almost the same trends of Cu; a relatively oxidized state drives a slightly faster drop of Ni at lower pressure (Fig. S3).

To address the behavior of Ni and Cu, a secondary operation was done on the output of alphaMELTS (Supplementary 3). There are two simple alternative models for the trace element distribution during partial melting (White 2013): equilibrium model based on the mass balance, or fractional model where the melt is extracted instantaneously without being equilibrated with the restite (Shaw 1970). It has been confirmed that the equilibrium partitioning model offers a good approximation of trace element behaviors in the complex partial melting reactions (e.g., Langmuir et al. 1993). For the finite difference models used here, the differences between Ni and Cu concentrations in the pooled melt derived from equilibrium and fractional (modal and non-modal) partitioning models are less than 3 ppm (Supplementary 3), and hence we adopted the simple equilibrium model where the contents and individual partition coefficients of the solid phases plus residual sulfide at each melting increment were used to calculate the instantaneous bulk partition coefficients. As the amount of residual sulfide is not provided by alphaMELTS, it must be calculated by mass balance, subtracting the amount of S dissolved in melt from the bulk S budget (Supplementary 3). Before the complete exhaustion of sulfide liquid in the source, melt in each increment is saturated with sulfide liquid, so the sulfur content of melt was obtained by using empirical SCSS parameterizations (Fortin et al. 2015; Smythe et al. 2017).

3.2 Adiabatic decompression melting of primary mantle in mantle plume

The decompression of mantle material is considered by some investigators to be essentially adiabatic (McKenzie and Bickle 1988; Asimow 1997). Alternatively, Herzberg and O’Hara (2002) advocated the importance of perfect fractional melting in plumes, which is different from adiabatic decompression because latent heat escapes with the extracted melt, and differs from continuous melting as there is no melt retained in restite after extraction. The impacts of adiabatic, perfect fractional or continuous melting on the compositions of primary melts have been evaluated in the Supplementary 4; Putirka (2016) argued that the differences between those three melting mechanisms would not introduce significant systematic errors. Here we use a model of purely adiabatic decompression melting, in part because the alphaMELTS software is not calibrated for pressures exceeding 4 GPa, preventing adequate modeling of open-system behaviour in high T_p mantle. In this purely adiabatic case the melt is not separated from the restite over the entire melting path.

To begin calculation of a melting path, the entropy of the metastable completely solid system is calculated at 0.1 MPa and the desired T_p. This estimated entropy will be unchanged along the adiabat, so it can be used as a constraint on the thermodynamic model at the starting point of the melting path to give the temperature of the stable assemblage at 4 GPa and then being held constant during decompression. Adiabatic upwelling of mantle leads to continued melting until upwelling ceases at the base of rigid lithosphere (Fig. 1). We have extended our decompression model to the surface in order to explore the effects of melt cessation under differing lithospheric thicknesses.

3.3 Isobaric melting of SCLM in plume-lithosphere interaction

The base of the lithosphere will be heated and weakened after hotter plume material impinges on it from below (Condie 2001; Manglik and Christensen 2006; Burov et al. 2007; Gorczyk et al. 2017). We examined the initial stage of plume-lithosphere interaction prior to any subsequent lithospheric thinning, so that the melting of SCLM is caused solely by the isobaric addition of heat from the plume.

For this isobaric melting model, we assumed pressures of 1.5, 2.7 and 3.9 GPa, corresponding to 45, 81 and 117 km thick lithosphere, respectively. Based on extensive calculations with oxybarometers in peridotites from the continental lithosphere, it has been concluded that the f_{O_2} of peridotites should decrease by 0.7 log units per 1 GPa increase in pressure (Foley 2010). Therefore, the appropriate f_{O_2} at these pressures are ΔFMQ = -1.0, -1.7, and -2.4, respectively. In addition, the estimated compositions of A-, P- and T-SCLM (Table 1) were adopted to take the evolution of lithospheric mantle into consideration (Griffin et al. 2009). The range of water contents of SCLM has been assumed as 0-300 ppm, whereas the water-rich portion (100-300 ppm) was used to examine the influence of metasomatism in melting of SCLM.

3.4 Flux-melting of mantle wedge above subduction zone

The presence of H_2O depresses the peridotite solidus, so the influx of slab-drived fluids and hydrous melts induces magmatism in the mantle wedge (Tatsumi and Eggins 1995; Stern 2002; Grove et al. 2012). Decompression melting associated with convection-induced pressure release has also been proposed to operate above subduction zones (Lee et al. 2009). Because decompression melting in subduction zones (e.g., Tatsumi et al. 1983; Plank and Langmuir 1988; Lee et al. 2009) is similar to what we already consider in mid-ocean ridges, the model here focuses on isobaric flux-melting in an open system, where the progressive addition of small amounts of H_2O and the removal of the generated melts occurs simultaneously at constant P-T close to the anhydrous solidus of mantle wedge peridotite. Primary magmas found in continental magmatic arcs typically last equilibrated with mantle at ~1 GPa and 1100°C, representing the crust-mantle boundary; while the temperature of the hottest part of mantle wedge even reaches ~1200-1350ºC (Grove et al. 2012). Therefore, the constant pressure in flux-melting model is assumed as 1.0 GPa, and the temperature of this open system ranges from 1100 to 1300 ºC. We modeled melting at a range of f_{O_2}, e.g., ΔFMQ = +1.0, +1.3, +1.6, +2.0.

In subduction zones, the compositions of slab-derived fluids vary from aqueous fluid (5-15% SiO_2 and 80-95% H_2O) to hydrous silicate melt (55-75 %SiO_2 and 5-30% H_2O) along subduction paths with rising pressure and temperature (Spandler and Pirard 2013). In addition, supercritical fluid, which exhibits complete miscibility between aqueous solution and hydrous melt, is predicted to form in subducting slabs at sub-arc depths (Spandler and Pirard 2013; Kessel et al. 2005a). In order to estimate the effect of various slab fluids on this flux-melting model, 15 typical fluid compositions from previous experiments were used to cover the variation range of these three fluid types (3 representative compositions are listed in Table 1) (Kessel et al. 2005b; Hermann and Spandler 2008). In this model, 0.1 wt. % slab-fluid is added into the system at each increment, and the portion of melt exceeding 1 vol. % is extracted and pooled to form the final magmatic output.

4. Results

4.1 Polybaric continuous melting of DMM

Figures 2 a-c exhibit the variations of Ni in aggregated melt during the partial melting of DMM at 1350ºC T_p. Ni concentrations decrease with increasing melting, which is opposite to expectations based on simple isobaric melting models (Naldrett 2010, 2011), as issue dealt with in the Discussion. Mantle source with greater H_2O contents (0 to 250 ppm) causes its partial melting to begin at a higher pressure (e.g., increase from 1.85 to 3.54 GPa in Figure 2a) and temperature, which diminishes the bulk Ni partition coefficient and therefore strongly elevates the Ni concentration within the first ~5 wt. % of melting (Figs. 2a, b and c). The effect of remaining melt fraction ("porosity") is felt most strongly at the initial stage of partial melting. If the DMM contains 250 ppm H_2O, the Ni concentrations in first instantaneous melt removed are 580, 543 and 511 ppm at the porosity of 0.3, 0.5 and 0.7 vol. %, respectively (Figs. 2a, b and c), because greater retention of the earliest Ni-rich melts occurs at higher porosity; these differences gradually decrease as melting progresses. In other words, greater proportions of retained melt modulate the effects of extreme first melt compositions. Based on the assumed initial S abundance (200 ppm) and potential temperature (1350ºC), the Ni in pooled melt produced by the polybaric continuous melting of DMM falls in a range between 320-450 ppm after 5 wt. % melting.

The trends of Cu in aggregated melt (Fig. 2d) also differ from previous results (Naldrett 2010, 2011; Lee et al. 2012; Ding and Dasgupta 2017). At anhydrous conditions, the Cu concentration of melt starts at 70 ppm, slowly grows to 87.1 ppm at 16-17 wt. % melting, and then declines. Addition of water will drive a great increase of Cu amounts in the first instantaneous melt (e.g., 94.6 ppm Cu at 250 ppm H_2O, Fig. 2d), which is followed by a sharp drop of Cu within the first ~0-3 wt. % melting. The variations of Cu in hydrous melt output are almost parallel to, but slightly higher than the result from anhydrous melting (Fig. 2d). Moreover, the influence of porosity (i.e., melt retention in the source) on the Cu concentration of melt is so small as to be negligible.

At 1350℃ T_p and 200 ppm initial S, the sulfide in residual mantle will be exhausted after ~11.7 wt. % melting, which should not be notably influenced by various water contents and remaining melt fractions. The Ni concentrations of residual sulfide liquids increase from initial values of ~27.5, 24.5, and 23 wt. % (at the initial H_2O contents of 0, 100, and 200 ppm, respectively) to 31.5 wt.% immediately before complete exhaustion of residual sulfide, and the Cu amounts range from 2.79, 2.55, and 2.41 wt. % (at 0, 100, and 200 ppm H_2O, respectively) to ~6.35 wt.% (Figs. 2a, b and c). Moreover, the MgO and FeO of melt output decrease continuously during partial melting (Figs. 2e and f); as with Ni, addition of water can strongly increase their contents at the initial stage.

Higher T_p leads to increased concentration of Ni in melt (~50-100 ppm with the 25℃ increase of T_p) over the whole partial melting path (Fig. 3a). Parallel effects of T_p on the MgO and FeO of aggregated melt are shown in Figure 3c and 3d. The increase of T_p will also drive Cu concentrations to higher values in melt outputs (rise of ~6-17 ppm for 25℃ increase of T_p), but this influence wanes after the complete exhaustion of sulfide (Fig. 3b). A hotter DMM brings about the exhaustion of sulfide at a greater depth and a lower melting fraction (Fig. 3a). Moreover, in Figure 2d and Figure 3b, the point when Cu reaches its maximum value slightly lags behind the exhaustion of sulfide in residual mantle due to the buffering of remaining melt, and a higher T_p will cause the maximum in Cu concentration to occur earlier and extend at a higher value.

4.2 Adiabatic decompression melting in Mantle Plumes

In the adiabatic decompression melting model, the Ni concentration in primitive melt also decreases with the increasing melting degree (Figs. 4a, c and e). Because the base of solid lithosphere limits the final depth of decompression melting of plume which, in turn, determines the extent of melting, the influences of distinct parameters on melt output are easiest to compare at a single pressure. At given pressure and T_p, H_2O in the source can strongly increase the melting fraction, and drive a slight or negligible decrease of Ni concentration in melts. For example, at the same pressure

(2.7 GPa) and potential temperature (1500℃), the decrease of Ni caused by 0-1000 ppm H_2O addition is ~26 ppm, whereas continued addition of 2000-6000 ppm H_2O causes a further drop of only 44-76 ppm Ni (Fig. 4a). By analogy to the polybaric continuous melting of DMM, the influences of water on melting fractions and Ni contents are weakened at high degrees of partial melting. On the other hand, small decreases in pressure cause large decreases in Ni, e.g., a fall of ~90-180 ppm Ni for a pressure drop of 0.6 GPa (Figs. 4a, c and e). In contrast, a higher T_p largely increases the degree of melting and slightly increases the Ni content of melt at the same pressure and water content, e.g., 876 ppm (T_p=1500℃), 966 ppm (T_p=1550℃) and 1011 ppm (T_p=1600℃) at 2.7 GPa and 0 ppm H_2O (Figs. 4a, c and e). Therefore, Ni concentration in primitive melt is more strongly affected by pressure than by an increase of T_p, and both of them far overweigh the effects of H_2O at the same pressure. Additionally, the exhaustion of sulfide in the source will be completed earlier in a hotter plume, changing from 21.4% to 16.1% melting for an increase of T_p from 1500℃ to 1550℃.

The MgO content of melt also decreases with melting until the exhaustion of orthopyroxene (Figs. 4b, d and f). After this point, the restite is dunite and further melting leads to rapid rise of MgO in melt. At constant pressure, the effect of H_2O addition on MgO is insignificant. Moreover, the pressure drop causes an obvious decrease of MgO, which is analogous to the trend of Ni in melt. Likewise, a higher T_p slightly increases the MgO of magma (~0.5-1.0 wt. %) at the same pressure and water content. In all, the trend of MgO within primitive melt is similar to that of Ni during adiabatic decompression melting process.

At T_p=1500℃, the Cu concentration in melt always exhibits a constant downward trend with increasing melting, and the exhaustion of sulfide causes only a slight inflection on the slope of Cu vs. degree of melting (Fig. 5a). This trend is different from either the long-held view of Cu behavior (Naldrett 2010, 2011; Lee et al. 2012; Ding and Dasgupta 2017) or the previous results obtained for polybaric continuous melting of DMM (Figs. 2d and 3b), and we return to this matter in the Discussion. Addition of water will drive a slight increase of Cu in melt at the same melting fraction, but this effect is negligible after the complete exhaustion of sulfide in source (Fig. 5a). In contrast, at constant pressure, a greater amount of H_2O in source slightly reduces the Cu concentration of primary melt (by ~6 ppm for 0 to 1000 ppm H_2O at 3.9 GPa) due to the extended degree of melting. Although sulfide exhaustion occurs at different melting degrees for T_p=1500 and 1550℃, the Cu concentrations of melts fall into equal or near-equal ranges from 0 to 4 GPa (Figs. 5a and 5b). In the model with higher T_p (>1600℃), the residual sulfide is entirely dissolved at greater depth before the simulation begins (i.e., >4 GPa), so its result only reflects the late diminishing part and overlaps the Cu trend for the 1500℃ T_p model at the corresponding melting range. Before complete exhaustion of sulfide, the Ni and Cu amounts of residual sulfide liquids fall into a narrow range (Ni, 24.7-30.8 wt. %; Cu, 1.8-2.29 wt. %) (Fig. 5).

4.3 Isobaric melting of SCLM due to plume-lithosphere interaction

For an isobaric melting model, the temperature of SCLM must be continuously increased to trigger and continue partial melting. Several numerical simulations of plume-lithosphere interaction have generated the temporal and spatial distribution of the complex resulting temperature field (Farnetani and Richards 1994; d'Acremont et al. 2003; Burov et al. 2007; Koptev et al. 2015; Gorczyk et al. 2017). To avoid endless proliferation of model parameters we have adopted a simple limiting constraint that the melting temperature in SCLM cannot exceed the temperature of subjacent plume. In Figure 6, the conditions where the continuously rising temperature of the isobaric model intersects with the temperature of adiabatic decompression melting at the same pressure, are indicated as round dots. If the temperature of the system exceeds this threshold value, the remaining parts of models will be divorced from reality, and shown as dotted lines.

The models of A-, P- and T-SCLM at 3.9 GPa, 50 ppm H_2O and ΔFMQ-2.4, show that Ni concentration increases steadily in melt as melting proceeds (Fig. 6a). Based on the assumed S abundances (Table 1), the residual sulfide of source is entirely dissolved in melts at ~1.43%, 5.76% and 10.14% melting for A-, P- and T-SCLM, respectively. Overall, at the same degree of melting, the relative Ni contents of melt from A-SCLM are highest, followed by P-SCLM and T-SCLM. The oldest A-SCLM should be strongly depleted and refractory after previous melting events. Thus, limited to the temperature threshold offered by the plumes with same T_p, the effective melting extent of A-SCLMs is lower than that of P-SCLMs, and both of them are lower than T-SCLMs (Fig. 6a). If S has not previously been affected by metasomatism of SCLM, the isobaric melting of SCLMs mostly ceases before the complete exhaustion of sulfide, except for the T-SCLM heated by mantle plume with 1600℃ T_p (Fig. 6a).

To examine the effect of lithospheric thickness, isobaric melting of T-SCLM has been modeled at 1.5 GPa (ΔFMQ-1.0), 2.7 GPa (ΔFMQ-1.7) and 3.9 GPa (ΔFMQ-2.4) (Fig. 6b). For the same source, isobaric melting at higher pressure results in higher Ni contents; melting at 2.7 GPa results in Ni contents ~400 ppm greater than at 1.5 GPa. Additionally, the reduction of pressure will also drive a slight delay for the sulfide exhaustion, and much higher degrees of melting occur at lower pressure (Fig. 6b). The MgO content of melts for different SCLMs and pressures have similar trends as the Ni concentration with the melting increases (Fig. 6c). Dotted lines in Figure 6c show the unrealistic increases in melt MgO content that would occur if the isobaric melting was not limited by the temperature of the impinging plume.

The Cu concentration of melt in isobaric model shows a rapid growth at the beginning of melting, followed by a smooth increase to a maximum value, and then a slow decline (Fig. 6d). The complete exhaustion of sulfide slightly lags behind the appearance of maximum Cu concentration, except in the case of partial melting of T-SCLM at 1.5 GPa. Higher pressure increases the Cu concentration at the initial stage of melting, but the results at different pressure overlap at higher degrees of melting after the exhaustion of sulfide (Fig. 6d). As the A- and P-SCLM may be depleted in Cu due to multi-phase magmatic events, the Cu released by their isobaric melting is generally less than that of T-SCLM at the same fraction of mantle melted (Fig. 6d).

Isobaric melting models of T-SCLM with different H_2O contents (0-300 ppm) were conducted under 3.9 GP and ΔFMQ-2.4, using H_2O as a proxy for the many possible fluxing influences of metasomatism. Because H_2O in the source reduces the melting temperature, its effect is exhibited in element concentration vs. temperature diagrams (Figs. 6e and f). The increase of H_2O from 0 to 300 ppm leads to only 11℃ drop of the temperature at which sulfide is exhausted (Figs. 6e and f). On the other hand, the influences of H_2O addition on the overall trends of Ni and Cu are insignificantly small. At the same temperature, just ~60 ppm growth of Ni concentration is related to the increase of H_2O from 0 to 300 ppm (Fig. 6e). The variation of melt productivity (%/℃) along with the increasing temperature shows a smooth growth at the onset of melting, and then rapidly increases to a maximum value with the exhaustion of clinopyroxene, which can be slightly delayed via the loss of H_2O (Fig. 6e).

4.4 Flux-melting of mantle wedge

Variations of Ni and Cu in the aggregated melt during the partial melting of mantle wedge are shown in Figure 7. Although the model slab-derived fluids cover the compositional range from aqueous fluid to hydrous silicate melt, these changes have little influence on the Ni, Cu concentrations and compositions of melts. Increase of temperature from 1100 to 1300 °C causes increases in MgO and Ni contents in magmatic output, e.g., 5-6 wt.% MgO, ~90 ppm Ni at 1100℃ and 11-13.5 wt. % MgO, ~250-300 ppm Ni at 1300℃ (Figs. 7a and b).

On the other hand, increasing temperature also enhances the transfer of S into the melt, leading to sulfide exhaustion at ~17 %, 19 %, 20.5 %, 21.3 % and 22 % of mantle wedge melted at the temperature of 1300, 1250, 1200, 1150 and 1100℃, respectively, which, in turn, will control the behavior of Cu during flux-melting (Fig. 7c). Moreover, the timing of maximum values of Cu lag behind the sulfide exhaustion owing to the buffering of remaining melt. Variations of initial S abundance in the source can slightly enhance or retard the exhaustion of sulfide, driving a little increase or decrease of the Cu maximum, but all trends overlap at high degrees of melting (Fig. 7d). The depleted DMM will reach the exhaustion of sulfide earlier, but the reason for these nearly parallel Cu trends is the different initial concentrations of Cu in sources (Fig. 7e). At higher f_{O_2}, sulfide will be exhausted at lower degree of melting because of enhanced S solubility, resulting in earlier and more efficient release of Cu into the melt. For example, the maximum value of Cu within melt exceeds ~170 ppm at ΔFMQ+2 and 1% melting, but is about 65 ppm for ΔFMQ+1 and 20% partial melting (Fig. 7f). More oxidized conditions are therefore conducive to the generation of more Cu-rich arc magmas from a given source.

5. Discussion

5.1 Partitioning behavior of Ni during decompression melting

Based on the models above, the distribution of Ni during partial melting of mantle is complicated and shows a strong dependence on tectonic setting (230-450 ppm Ni for mid-ocean ridges, Figs. 2 and 3; 500-1300 ppm Ni for mantle plume, Fig. 4; 100-300 ppm Ni for subduction zones, Fig. 7), which can be attributed to the following reasons: (1) Ni is not only strongly compatible in sulfide, but is also hosted in major mineral phases in the source, especially the olivine which constitutes a large percentage of mantle and has a moderate partition coefficient for Ni (~1.5-13); (2) partition coefficients of Ni between the mineral phases and silicate melt are dependent on melt composition, pressure and temperature (Beattie et al. 1991; Li and Ripley 2010; Herzberg et al. 1991; Matzen et al. 2013, 2017a), which will change during the generation of magma; (3) source compositions, thermal regimes and melting mechanisms of mantle are different in various tectonic settings (Arndt et al. 2005), resulting in diverse melt products.

First of all, the partitioning behavior of Ni in mantle melting is determined by the bulk partition coefficient of Ni between restite and melt (D_{Ni}^{bulk}), which is simply the sum of the individual partition coefficients multiplied by the proportions of each phase, including the residual sulfide. Therefore, the variations of partition coefficients and modal phase proportions in restite during partial melting of mantle affect the Ni contents of melts along melting paths. As shown in Supplementary Figure S6, the contribution of olivine to the bulk partition coefficient is far greater than that of other phases, occupying ~ 78-91% proportion of D_{Ni}^{bulk} in the polybaric continuous melting of DMM (Fig. S6b), ~ >73% proportion in the adiabatic melting of PM (Fig. S6d), ~ 76.5-86% proportion in the isobaric melting of T-SCLM (Fig. S6f), and > 73.5% proportion in the flux melting of mantle wedge (Fig. S6h). Additionally, as garnet, clinopyroxene and/or orthopyroxene are exhausted in turn, the olivine proportion in restite rises in a similar manner over melting paths in different tectonic settings (Figs. S6a, S6c, S6e and S6g). Therefore, the distinct partitioning behaviors of Ni (Figs. 2, 3, 4, 6 and 7) are mostly strongly attributed to the variations of $D_{Ni}^{ol/melt}$ at different melting scenarios.

During decompression, for both the continuous melting of DMM and adiabatic melting of PM, Ni concentrations in melts decrease with increasing degree of melting (Figs. 2, 3 and 4), which contradicts intuition and the long-held conclusions derived from previous isobaric melting models with fixed partition coefficients (Naldrett 2010, 2011). As the D_{Ni}^{bulk} is mostly controlled by the partition coefficient between olivine and melt (Figs. S6b, S6d, S6f and S6h), the reasons for the distinct Ni trends are related to variations of $D_{Ni}^{Ol/melt}$ between melting scenarios. First, there is an obvious inverse relationship between $D_{Ni}^{Ol/melt}$ and MgO in melt (e.g., Hart and Davis 1978); the increasing temperature and pressure of melting typically yield primary melts with elevated MgO (Herzberg et al. 2013, 2016), and this strong correlation makes it difficult to distinguish the isolated effects of temperature and/or pressure on $D_{Ni}^{Ol/melt}$. More recently, the experiments of Matzen et al. (2013, 2017a) separated the influences of temperature from liquid composition, and demonstrated that the increase of temperature at constant melt composition largely decreases $D_{Ni}^{Ol/melt}$. Niu et al.

(2011) suggested explicitly the inverse correlation of $D_{Ni}^{Ol/melt}$ with increasing pressure, but this parameterization may not be consistent with the experimental database (Herzberg et al. 2013). In addition, an explicit pressure dependence is absent from many parameterizations of $D_{Ni}^{Ol/melt}$ (Li and Ripley 2010; Putirka et al. 2011; Herzberg et al. 2013); Matzen et al. (2013, 2017a) proposed that the effect of pressure on $D_{Ni}^{Ol/melt}$ is negligible over the range from 0 to 3 GPa. Incorrect results are obtained by simple isobaric melting models because increasing temperature and continuous growth of MgO in melt cause a decrease of $D_{Ni}^{Ol/melt}$ in isobaric models (Naldrett 2010, 2011). For the decompression melting of mantle, the variation of pressure cannot be ignored, and will exert a strong influence on the melt composition. Melting experiments of both the spinel peridotite and garnet peridotite have consistently shown that MgO increases in partial melt with the increasing pressure (Jaques and Green 1980; Walter 1998; Herzberg and Asimow 2015). Once upwelling mantle material intersects the solidus, initial melting occurs at the largest pressure and, in turn, results in minor melt production of melt with the highest MgO. As upwelling continues, more melt with less MgO will be generated at lower pressure, which dilutes the original high-MgO melt. Hence, the drop of pressure in decompression process causes the decrease of MgO with melting before the exhaustion of orthopyroxene, resulting in rising $D_{Ni}^{Ol/melt}$ and a consequent drop of Ni concentration in the melt. In addition, the temperature of hotter mantle decreases during its ascent, making secondary contributions to the increase of $D_{Ni}^{Ol/melt}$ and decrease of Ni concentrations in the decompression of DMM and PM (Matzen et al.

2013, 2017a). This trend of MgO within melt has also been revealed by the accumulated and instantaneous fractional melts during adiabatic decompression paths of the fertile peridotite (Fig. 8 and Fig. 11 in Herzberg and O`Hara 2002).

5.2 Partitioning behavior of Cu during partial melting

In consideration of the complexities of various melting degrees and source compositions, our results are in good agreement with existing knowledge of the Cu concentrations in MORBs (60-90 ppm), arc basalts (50-100 ppm) and OIBs (80-120 ppm) (Fellows and Canil 2012; Lee et al. 2012; Liu et al. 2014; Richards 2015). Based on the recent experimental investigations on the partition coefficients of Cu between mineral phases and silicate melts at upper mantle conditions (Fellows and Canil 2012; Lee et al. 2012; Liu et al. 2014; Le Roux et al. 2015; Zhang et al. 2017), many models for the partitioning of Cu within partial melting have reached a consensus that its concentration increases with progressive melting at initial stage, reaches a maximum value and then starts to decrease when sulfide is exhausted as there is little to hold them back in the restite (Naldrett 2010, 2011; Lee et al. 2012; Zhang et al. 2017; Ding and Dasgupta 2017).

However, our models predict some distinct and complex partitioning behaviors of Cu during the partial melting of DMM (Figs. 2d and 3b), PM (Fig. 5), SCLM (Fig. 6d) and mantle wedge (Figs. 7c-f), which is mostly attributed to the new insight into $D_{Cu}^{sul/melt}$. Due to the insufficient and unsystematic experiments on $D_{Cu}^{sul/melt}$, a high constant value was mostly used as a simplifying assumption in previous models (e.g., 800 in Lee et al. 2012, 1000 in Ding and Dasgupta 2017), which ignores the possible effects of changes of $D_{Cu}^{sul/melt}$ and overestimates the contribution of sulfide to the D_{Cu}^{bulk}. More recently, Li and Audétat (2012) recognized that the sulfide-silicate melt partition coefficients of Ni and Cu vary as a function of oxygen fugacity. Then Kiseeva and Wood (2013, 2015) did further experiments and developed a more comprehensive thermodynamic model that takes account of the effects of temperature, oxygen fugacity (refers to the FeO wt. % in silicate melt) and the composition of sulfide liquid on $D^{sul/melt}$, to describe the Ni and Cu partitioning between sulfide liquids and silicate melts. A simple relationship between the $D_{Cu}^{sul/melt}$ and the FeO of melt has been confirmed by Kiseeva and Wood (2013), showing the negative near-linear correlation in diagram of $\log D_{Cu}^{sul/melt}$ vs. $\log FeO$. Moreover, negative T-dependences were also observed within the range of 1300-1700ºC, and substantial addition of Ni and/or Cu into the sulfide liquid resulted in the slight variation of $\mathrm{D}^{sul/melt}$ (Kiseeva and Wood 2015). As a result, the elevated temperature and FeO of melt experienced during melting at higher pressure drive an important reduction of $D_{Cu}^{sul/melt}$.

Walter (1998) demonstrated that the FeO of melt increases with increasing pressure, although his data exhibit considerable scatter. Hence, the FeO of melt output during decompression, shows a sustained downward trend (Fig. 3d), leading to the increase of $D_{Cu}^{sul/melt}$ (Fig. 8a) and falling Cu of melts. On the other hand, the ascent of mantle is also accompanied by the reduction of temperature, which also makes a secondary contribution to the elevated $D_{Cu}^{sul/melt}$. As the start of melting for the hotter mantle occurs at a higher pressure, the $D_{Cu}^{sul/melt}$ will increase from a lower value for the mantle partial melting at a larger T_p. For the adiabatic decompression melting of mantle plume (T_p>1500℃), the values of $D_{Cu}^{sul/melt}$ are always smaller than ~290 before the exhaustion of residual sulfide (Fig. 8a), resulting in the monotonic decrease of Cu with melting (Fig. 5). Similarly, Cu concentrations during polybaric continuous melting of DMM at T_p= 1400 and 1375℃ will also exhibit a fast drop followed by a smooth increase (the concave trend of Cu before exhaustion of sulfide, Fig. 3b) because their increasing $D_{Cu}^{sul/melt}$ cross the transition value (~360) for Cu evolution above which its D_{Cu}^{bulk} becomes less than unity (Fig. 8a). In contrast, for lower T_p cases, Cu mostly increases before sulfide is exhausted (Fig. 3b) as their values of $D_{Cu}^{sul/melt}$ always exceed ~360 (Fig. 8a). Additionally, because of the relative low $D_{Cu}^{sul/melt}$ at the initial melting of DMM, the Cu content begins the melting path at moderate values, which is distinct from the low initial value of Cu predicted by previous models (Naldrett 2010; Lee et al. 2012; Ding and Dasgupta 2017). As a result, the Cu contents of melts derived from partial melting of DMM fall into a narrow range (~60-90 ppm for 1300-1375℃ T_p) during the entire decompression process, matching well with the observed distribution of Cu from MORB worldwide (Fellows and Canil 2012). The hotter plume results in a very low value of $D_{Cu}^{sul/melt}$, which, in turn, increases the Cu of primary melt, showing good agreement with the relative high Cu contents from OIBs (Fellows and Canil 2012).

In contrast, the constantly rising temperature within isobaric melting of SCLMs induces the increase of FeO of melt output, meanwhile both factors cause the reduction of $D_{Cu}^{sul/melt}$. Its low melt productivity (%/℃) at the initial stage of partial melting (Fig. 6e) determines that ~2-3% fraction after the onset of melting requires great growth of temperature, leading to a sharp drop of $D_{Cu}^{sul/melt}$ (Fig. 8b) accompanied by the rapid increase of Cu abundance in this stage (Fig. 6d). Then the trend of $D_{Cu}^{sul/melt}$ shows a smooth decrease due to the relatively slow heating process (moderate melt productivity, Fig. 6e) at the high melting fraction (Fig. 8b). Additionally, the positive relationship between pressure and FeO content of melt also makes a difference, showing that the isobaric melting of T-SCLM at higher pressure produces melt with higher FeO content, lower $D_{Cu}^{sul/melt}$ and consequently higher Cu content (Figs. 8b and 6d). At 3.9 GPa, the $D_{Cu}^{sul/melt}$ falls beneath ~150 for Cu evolution during isobaric melting, leading to the transition of Cu abundance from fast initial rise to smooth decrease (Fig. 6d). Hence, during the isobaric melting of SCLMs at high pressure, the control of mantle sulfide on Cu partitioning behavior is weakened by the sustained fall in $D_{Cu}^{sul/melt}$, and the maximum Cu content in the melt can be reached before the exhaustion of sulfide within the restite.

As the temperature and pressure are constant within the flux-melting model, the FeO content of melt output is nearly invariable, producing little change in $D_{Cu}^{sul/melt}$ during partial melting (Fig. 8c). Increasing temperature causes an increase in FeO and reduction of $D_{Cu}^{sul/melt}$, but all the flux-melting models at appropriate temperature range (1100-1300℃) confirm the high level of $D_{Cu}^{sul/melt}$ (>~590), driving the monotonic increase of Cu concentration with increasing melting before sulfide exhaustion (Figs. 7c-f), which is parallel to the Cu trends from previous models with the assumed high $D_{Cu}^{sul/melt}$ (Naldrett 2010, 2011; Lee et al. 2012; Ding and Dasgupta 2017).

5.3 Composition of base metal sulfide

Base metal sulfide (BMS) within the mantle has drawn attention because it controls the behaviors of chalcophile and siderophile elements and plays a crucial role in recording melt depletion, enrichment and/or metasomatic events that may occur in the mantle, particularly for Re-Os isotope systematics (Lorand and Luguet 2016; Harvey et al. 2016). We presume that under all conditions addressed in our modeling study, the BMS exists as a single sulfide liquid phase (Zhang and Hirschmann 2016).

Here, the thermodynamic model for Ni and Cu partitioning between sulfide and silicate melt (Kiseeva and Wood 2013, 2015) not only traces the variations of $D_{Ni}^{sul/melt}$ and $D_{Cu}^{sul/melt}$, but also provides a new insight into the compositional evolution of BMS during partial melting of mantle. During the polybaric continuous melting of DMM, the Ni concentration in BMS increases from 27.5 to 31.7 wt.%, along with the rise of Cu from 2.79 to 6.33 wt.% (Figs. 2a, b and c). Addition of water to the source drives a slight reduction of Ni and Cu contents in low-degree melting due to the H_2O-induced extremely low $D^{sul/melt}$ at the onset of melting (Fig. 2f). For the adiabatic decompression melting of hotter mantle, BMS falls into a similar range for Ni abundance (24.7-29.9 wt.%), but a relatively lower and narrower range for Cu concentration (1.8-2.3 wt.%, Fig. 5). In contrast, the BMS in models of isobaric melting of SCLM exhibits decreasing Ni and Cu concentrations with increasing melting (Fig. 6d), because of the drop of $D^{sul/melt}$. The ranges of Ni and Cu in BMS are larger if the SCLM melts at lower pressure, and the melting of strongly-depleted A-SCLM at 3.9 GPa results in Ni-rich, Cu-poor BMS (Fig. 6d). Flux-melting of the mantle wedge gives a wide range for the composition of BMS that mostly has high Ni (20-36 wt.%) and Cu (2-15 wt.%). In all, the sulfide compositions within our models mostly fall into the range of 20-30 wt.% Ni and 2-10 wt.% Cu, coinciding well with the observed compositional range of peridotite-hosed sulfide worldwide (e.g., Guo et al. 1999; Wang et al. 2009; Liu et al. 2010; Lorand and Luguet 2016; Harvey et al. 2016). Although the influence of Ni and Cu concentrations in sulfide on partitioning is relatively small (Kiseeva and Wood 2013, 2015), their impacts on the SCSS model are the factors that must be considered (Ariskin et al. 2013; Smythe et al. 2017).

We have used our modeled phase compositions to assess several published parameterizations for the distribution of Ni between olivine and sulfide melt (Supplementary 5). Whereas our model results are consistent with experimental data in olivine-sulfide systems, they are not consistent with any of the published models. We conclude that there is potential to derive a self-consistent model for olivine-sulfide partitioning of Ni from the existing thermodynamic models for olivine-silicate melt and sulfide liquid-silicate melt partitioning that would be more accurate than the existing ones (e.g., Barnes et al. 2013; Sciortino et al. 2015).

5.4 Effect of lithosphere thickness overlying mantle plume

The decompression melting of deep-rooted thermal mantle plumes is triggered by their intersection with the solidus, during the adiabatic upwelling of plume mantle, and ceases at the bottom of lithosphere (Fig. 1). Hence, the base of rigid, nonconvecting lithosphere will act as a 'lid' on upwelling sources, controlling the vertical range of decompression processes, which is also proportional to the extent of melting (Humphreys and Niu 2009; Niu et al. 2011). This decompression melting beneath thick lithosphere stops at a greater depth, resulting in less melt with a high pressure signature; whereas more melt bearing a low pressure signature comes from partial melting beneath thin lithosphere (Humphreys and Niu 2009; Niu et al. 2011). Because high pressure leads to the lower melting degree, larger MgO and Ni in melt (Fig. 4), the lithosphere thickness exerts a strong control on the Ni concentration of mantle plume-derived magma. On the other hand, our results are consistent with explanations for the occurrence of high-Ni olivine phenocrysts stating that the presence of thick lithosphere leads to high Ni contents in melt that in turn, allow the crystallization of Ni-rich olivine near the surface (Niu et al. 2011; Putirka et al. 2011; Matzen et al. 2013, 2017a, b).

It has been confirmed that variation of oceanic lithosphere thickness exerts the first-order control on the major elements of OIBs (Humphreys and Niu 2009; Niu et al. 2011). We have adopted geochemical data for volcanic islands from the GEOROC database to evaluate the relationship between the lithosphere thickness and Ni concentration in melt. The samples with SiO_2>53% and no Ni contents were excluded, which resulted in a smaller data set containing 93 volcanic islands and 7216 samples from the Pacific, Atlantic and Indian Oceans. The Ni contents of the OIB data set were corrected for fractionation effects using the MORB liquid lines of descent (LLD) to $Mg^{\#}$=0.72 (Supplementary 6). In order to test the influence of lithosphere thickness, the corrected Ni contents of samples from each volcanic island were averaged (Supplementary Table S1). Lithosphere thickness of each volcanic island was obtained from Humphreys and Niu (2009), and given in Supplementary Table S1. Although it has large compositional scatter for a given volcanic island (1σ variation in Supplementary Table S1, and the error bars in Figure 9), the positive correlation of island-averaged Ni with lithosphere thickness is noticeable (R^2=0.295, Fig. 9), coinciding with the model-based prediction that termination of melting paths at higher pressure under thicker lithosphere results in the increase of Ni concentration in melt output.

Additionally, based on the GEOROC database, ultramafic-mafic volcanic samples from oceanic LIPs were also used to verify the effect of lithosphere thickness. Oceanic plateaus form in deep-ocean basins as broad and flat-topped plateaus with over-thickened crusts (Ernst 2014). Although some features of oceanic plateaus (in particular, Ontong Java) disagree with expectations of the mantle plume hypothesis (Korenaga 2005), most oceanic plateaus still appear to have formed as a result of decompression melting of a large mantle plume head (Révillon et al. 2000; Weis et al.

2002; Ernst 2014). The geochemical signatures of the Caribbean, Kerguelen and most Ontong Java oceanic plateau lavas show no evidence of lithospheric interaction (Kerr and Mahoney 2007; Ernst 2014). The older Kerguelen plateau basalts are slightly contaminated by continental lithosphere (Ingle et al. 2002), and Wrangellia is the only known oceanic plateau to have evidence for interaction with a subduction-modified lithosphere (Greene et al. 2008). Thus, most oceanic plateaus are unlikely to be modified by crustal contamination and continental lithosphere, and hence, are more useful than continental LIPs to decipher mantle processes and source materials (Kerr and Mahoney 2007; Ernst 2014). The Ni and MgO concentrations in lavas from oceanic plateaus show a strong positive correlation, especially when MgO exceeds 12 wt.% (Fig. 10a). Final melting pressure and temperature are inferred from the compositions of high-Mg rocks (>12 wt.%) following the equations from Herzberg and Gazel (2009) (Fig. 10b). Melting in the Ontong Java and Wrangellia oceanic plateaus is inferred to have ceased at 0.5-2 GPa, whereas the final melting pressures of Caribbean and Kerguelen magmas decreased from ~7 GPa to 0.5 GPa. Diameters of circles in Figure 10b are proportional to the Ni concentrations in samples. Although the rocks are mixtures of melts and olivine phenocrysts, causing some overestimations of Ni amount in melt, it appears that, in general, low final melting pressure leads to a relatively low Ni content (Fig. 10b).

Even if the parental magma for Ni-Cu-(PGE) deposit experiences ascent, assimilation, transport and crystallization after its generation (Naldrett 2010, 2011), a Ni-rich primary melt still has greater potential to form a deposit during its subsequent evolution. Based on many systematic studies of magmatic sulfide deposits, it has become widely accepted that most of them are closely related to the coeval mantle plume events and LIPs (Barnes and Lightfoot 2005; Begg et al. 2010; Qin et al. 2011; Ernst 2014; Barnes et al. 2015), e.g., the Noril'sk magmatic deposit associated with the end-Permian Siberian Traps (Lightfoot and Keays 2005). However, there is almost no significant Ni-Cu-(PGE) mineralization in oceanic LIPs, except the Wellgreen deposit in the Wrangellia plateau, which has interacted with the continental crust or lithosphere (Marcantonio et al. 1994; Ernst 2014). Our models indicate that melting beneath the thin oceanic lithosphere (mostly <90 km) may cause Ni concentrations too low to generate significant magmatic mineralization. Although the continental LIPs usually interacted with thick ancient cratonic lithosphere, there are still some barren continental LIPs, in which no significant magmatic Ni-Cu-(PGE) deposits have been found, e.g., the Paraná-Etendeka Province and Deccan Traps (Zhang et al. 2008). In the main pulse of Deccan Traps magmatism (~65 Ma), the thickness of Dharwar Carton in Indian may have been just ~80 km (Dessai et al. 2004; Karmalker et al. 2009). Based on the compositions of MgO-rich rocks, most magmatism in the Deccan LIP was constrained by its low lithosphere thickness, and contain extremely low Ni contents (8-573 ppm, Zhang et al. 2008). Additionally, a thinned lithosphere is also advocated in the Paraná-Etendeka LIP event (Gibson et al. 2006). The thin lithosphere may therefore be one of the reasons for the barren Deccan and Paraná-Etendeka LIPs. However, it must be recalled that the mineralization process depends on a combination of factors such as the availability of S-rich crustal contaminants and suitable structural traps that are not related to the composition of the primary magma; furthermore, not all valuable Ni deposits are preserved and exposed where we can find them. Absence of evidence for their existence is not evidence of their absence.

5.5 Effect of potential temperature in mantle plume

Besides lithosphere thickness, the potential temperature also influences the P-T condition at which melting ceases within the ascending plume. Evidently T_p of an adiabatically upwelling plume must be high enough for it to intersect the solidus at sub-lithospheric depths (e.g., Farnetani and Richards 1994; Garfunkel 2008). At constant pressure (e.g., thickness of lithosphere lid), a 50℃ increase of T_p will lead to ~2 MgO wt. % growth and ~70-110 ppm Ni increase in melt.

The T_p of some typical oceanic and continental LIPs have been calculated using PRIMETL 3 (Herzberg and Asimow 2015) (Fig. 11). In our calculations, we excluded samples: (1) generated from pyroxenite sources; (2) degassed from CO_2-rich sources; (3) which have experienced plagioclase and/or clinopyroxene fractionation. All results illustrated that LIPs were formed by sources which are hotter than normal mantle, and most of them have a wide range of T_p, such as 1410-1670℃ for Siberian Traps (Fig. 11). Although secular cooling does occur in mantle plumes (Herzberg and Gazel 2009), this influence is very small for the short duration of these LIP events, and hence, the variations of T_p mostly depend on the thermal structure of mantle plume such that hot primary magmas originate from the axis with high T_p, and cooler primary magmas come from the periphery having low T_p (Ribe and Christensen 1999). Therefore, the primary melt related to the highest T_p in plume-center should have great ore potential, coinciding well with observations that the Ni-Cu-(PGE) mineralization is usually proximal to their respective mantle plume centers (Ernst 2014). Furthermore, Lee et al. (2009) concluded that Archean komatiites mostly formed by melting in a mantle with a T_p>1700℃, which is one of the possible reasons for the abundant magmatic Ni-Cu-(PGE) sulfide deposits located in komatiites.

5.6 Effect of H_2O in Mid-Ocean Ridges and Mantle Plumes

Under water-unsaturated conditions in our models, the effect of H_2O on mantle melting was determined via a simplified approach using water partition coefficients between phases and melt (Asimow et al. 2004; Hirschmann 2006), where water as an incompatible component has a strong tendency to enter into the melt. The decreased melting temperature of hydrous mantle causes the onset of melting at a higher pressure (Fig. 1) (Hirth and Kohlstedt 1996; Asimow and Langmuir 2003; Aubaud 2004), which further results in a series of changes in the melt composition, e.g., the reduction of SiO_2 and increase of MgO and FeO (e.g., Hirose and Kushiro 1993; Hirose and Kawamoto 1995; Walter 1998). The elevated MgO causes a decrease of $D_{Ni}^{Ol/melt}$ (Matzen et al. 2017a), resulting in an increase of Ni concentration in the melt. Meanwhile, the increase of FeO content will also reduce $D_{Cu}^{sul/melt}$ (Kiseeva and Wood 2013, 2015), facilitating the liberation of Cu into the melt. Additionally, recent experiments demonstrate an increase in the SCSS of ~100 ppm/wt.% added water into the melt composition (Fortin et al. 2015), which enhances the dissolution of residual sulfide to release more Ni and Cu at the same melting degree. Therefore, the influence of water on mantle melting can be projected on the partitioning behavior of Ni and Cu, and mostly will elevate their concentrations in the melt output.

During polybaric continuous melting of DMM, the augmenting effects of water addition on the Ni and Cu concentrations are significant at the initial stage, but will be gradually weakened with continued melting (Figs. 2a-d). As the bulk partition coefficient for hydrogen applicable to partial melting of mantle is extremely low (~0.009) and similar to that of incompatible Ce (Aubaud 2004; Kohn 2006), hydrogen should be strongly concentrated in melt. Because of the very small amount of water contained in DMM, its abundance within the source will be diluted by further melting and has little effect on the maximum melting extent (Hirth and Kohlstedt 1996; Asimow and Langmuir 2003). On the other hand, although H_2O can trigger the onset of partial melting at higher pressure, the melt productivity (%/GPa) is extremely low at the initial stage. Hence, the addition of water strongly expands the melting region by creating a large pressure interval at the base of the main melting regime, but the contribution of this elongated area to the final melt output is minimal (Asimow and Langmuir 2003). Therefore, the sharp drop of Ni and Cu concentrations within 0-3 wt.% melting (Figs. 2a-d) comes from the accumulated effect of a long decompression path with the very low melt productivity.

However, the net effect of water addition seems to be long-lasting in the adiabatic decompression melting of primary mantle (Figs. 4 and 5). In addition to the differences between the initial abundance of H_2O within PM (0-6000 ppm) and DMM (0-250 ppm), the partial melting mechanisms can also make some difference. In the polybaric continuous melting and perfect fractional melting, H_2O is lost rapidly from the system but this loss of water is not experienced during adiabatic decompression melting. Notwithstanding the fact that water addition can drive the increase of Ni and Cu contents at the same melting fraction; at a constant pressure (lithosphere thickness), the increase of water from 0 to 1000 ppm slightly decreases the Ni and Cu in melt (Figs. 4 and 5) because the melting extent has been greatly increased. In adiabatic decompression melting, this influence of water will also become negligible at high melting fraction.

Ductile delamination of continental lower lithosphere can cause continental magmatism, possibly with large volumes (Elkins-Tanton 2005, 2007; Lustrino 2005). The delaminating material may dehydrate as it sinks and heats, releasing a fluid that induces melting in the asthenospheric mantle which has flowed in to replace the foundered lithosphere; furthermore, the rising asthenosphere may produce melt adiabatically in response to the upward movements (Elkins-Tanton 2005; Lustrino 2005). However, delamination models do not require hotter mantle upwelling from deep hotter boundary layers, and hence the adiabatic decompression melting occurs within ambient normal mantle (~T_p=1350℃). The model of DMM melting in mid-ocean ridge, shows that the metals in melt remain at a relatively low levels under such conditions (Ni, ~230-450 ppm; Cu, ~60-90 ppm). Moreover, the addition of vast amounts of water to the source (e.g., 2000-6000 ppm) in adiabatic decompression greatly increases its melting extent and causes reductions of Ni and Cu in melt at the same pressure (Figs. 4a, c, e, and 5). The overall combination of decompression- and fluid-induced melting provoked by the lithospheric delamination undoubtedly can generate extensive magmatism, but the metals in the melt output are far lower than that in mantle plume-related suites.

5.7 Contribution of SCLM to plume-derived magmas

Recently, the contribution of SCLM to the mineralization in magmatic ore deposits has been a topic of much discussion and debate. Griffin et al. (2013) claimed that 'fertile' (mineralized and continental) LIPs with high PGE contents (e.g., at the Bushveld Complex) have a close genetic relation to the SCLMs. Mungall and Brenan (2014) also advocated a mixture of SCLM- and asthenosphere-derived magmas to account for the PGE composition of Bushveld magmas. However, Arndt (2013) suggested that lithospheric mantle may play no active role in the magmatic deposits, and no evidence was found for systematic differences in magma compositions between various LIPs that could be attributed to contributions from SCLM (Barnes et al. 2015).

From the T-SCLMs to P-SCLMs and then to A-SCLMs, the lithospheric mantle is continuously depleted due to the progressive removal of basaltic components during previous partial melting events, resulting in high Mg number, slight increase of Ni content, obvious reduction of Cu and S concentrations, and small amounts of easily fusible minerals (Griffin et al. 1999, 2009; Arndt 2013; Wang and Becker 2013, 2015). Hence, A-SCLM requires a higher temperature for a lower melting degree, and the contributions of Ni and Cu from older lithospheric mantle to plume magmas must be rather small, although A-SCLM-derived melts may have a slightly higher Ni content (Fig. 6a) but lower Cu concentration (Fig. 6d). In all isobaric melting models of SCLMs, the Ni and Cu amounts in melt are always less than that in corresponding plume system driving heating of the SCLM, even at the maximum extent of SCLM melting. Mixture of melts generated from SCLMs and plumes undoubtedly contributes continental signatures, but this process dilutes the Ni and Cu in the plume-related primary melt. Furthermore, our model did not account for the drop of temperature during plume-lithosphere interaction, heat loss by conduction and the complexities of the spatial thermal regime in SLCM. Hence, the achievable degree of melting in the SCLM was overestimated here. Once the sulfide in SCLMs has been completely dissolved, which is not likely to occur for the A-SCLMs and P-SCLMs in our models (Fig. 6a), it is possible that a unique SCLM PGE signature may be imparted to the mixed asthenosphere-SCLM source melt (Mungall and Brenan 2014), however this is not expected to be important except in the hottest and largest plume impingement events such as the Bushveld LIP or cases in which large-scale refertilization of the SCLM by melts or fluids permits greater degrees of melting than are envisaged here. For the T-SCLM, sulfide exhaustion requires high T_p plume or thin lithosphere (Figs. 6a and b), which occurs when plume heads migrate towards the thinned edges of continental lithosphere but not within continents. Even if sulfide is exhausted, the Cu contents still stay in the same order with these in plume-related melt, showing no great enrichment. Although the addition of metasomatic fluids easily triggers SCLM melting, its influence on Ni and Cu is still minimal (Figs. 6e and f). Finally, there is little evidence that the metasomatized SCLMs are abnormally enriched in chalcophile and highly siderophile elements (Arndt 2013; Wang and Becker 2015; Aulbach et al. 2015; Barnes et al. 2015; Lorand and Luguet 2016) to increase the metals contents in their melting products. Therefore, during plume-lithosphere interaction, the contribution of SCLMs to the ore potential of mantle-derived magma output is minimal, or even negative.

5.8 Controlling factors in melting of the mantle wedge

For the partial melting of the mantle wedge above subduction zones, our flux-melting model is more suitable than the widely-adopted melting calculation (Lee et al. 2012; Liu et al. 2014; Le Roux et al. 2015) that assumed mineral phases and only changed melt fractions during the entire melting process. Our models confirm that the MgO and Ni contents of melts driven by flux melting in subduction zones are strongly enhanced by increases in temperature (Fig. 7a and b). High temperature will also drive increasing Cu concentration in melt (Fig. 7c) owing to its combined influences on SCSS and $D_{Cu}^{sul/melt}$, which may be one of the reasons for the elevated Cu content in the Cascade magmatic arc that is an example of a 'hot' subduction zone

(Fig. 2c in Lee et al. 2012).

Recent experiments confirmed that fluid-present melting of sulfide-bearing ocean crust enhances the transport of S from the slab to mantle wedge (Jégo and Dasgupta 2013, 2014). Sulfur enrichment leads to the complete exhaustion of residual sulfide at a higher melting fraction accompanied with a lower Cu maximum (Fig. 7d). On the other hand, melt induced by aqueous fluid has slightly larger MgO, Ni and Cu than the output triggered by hydrous silicate melt (Figs. 7a, b and c), ignoring any possible transfer of metals into mantle wedge by slab-induced fluids.

A simplified petrological model from Arai and Ishimaru (2008) demonstrated that before metasomatism, the degree of depletion of mantle peridotite decreases from the fore-arc to back-arc region within the mantle wedge. Although prior melt depletion would reduce S and Cu concentrations, the subsequent addition of slab-derived fluids may compensate the S depletion (Jégo and Dasgupta 2013, 2014). Hence, for the flux-melting of mantle wedge with different depletion degrees, the partitioning behaviors of Cu are more affected by the loss of Cu relating to the prior melt extraction rather than the variations of other major compositions (Fig. 7e), if the S content within mantle wedge remains the same. Additionally, the Cu enrichment in melt could potentially be derived from highly oxidized melting of the subducted slab (Oyarzun et al. 2001) and/or heating of pyroxenite cumulates in the deep roots of arcs (Lee et al. 2012), which may introduce more complexity into the behavior of Cu in the fore-arc and back-arc regions.

Oxygen and sulphur fugacity within the mantle wedge are also crucial to the fate of S and, in turn, the partitioning behavior of Cu during partial melting (e.g., Mungall et al. 2005, 2006; Jugo et al. 2010). It has been confirmed that a small increase in f_{O_2} above ΔFMQ+1 will have a strong impact on S behavior (transition from S^{2-} to S^{6-}), leading to a 10-fold increase of the total S solubility (Li and Ripley 2009; Jugo et al. 2010). Flux-melting of highly oxidized mantle wedge accelerates the liberation of Cu with the largest maximum value (~185 ppm Cu at ΔFMQ+2, Fig. 7f) owing to the low melting degree at the complete exhaustion of sulfide. However the influence of high oxidation state on Cu behavior is weaker than predicted by Lee et al. (2012), e.g., the Cu maximum value decreases from ~280 ppm to ~140 ppm (Fig. 7f) at ΔFMQ+1.6. At still higher f_{O_2}, Cu and other chalcophile elements are incompatible from the very onset of melting because sulfide melt is not a stable phase (e.g., Mungall 2002; Botcharnikov et al. 2013). Relatively high oxidation states are indicated in many arcs (Arai and Ishimaru 2008; Frost and McCammon 2008), but unlike Au and PGE (Mungall et al. 2006; Botcharnikov et al. 2013), no convincing correlation between magma oxidation state and Cu enrichment has been found (Lee et al. 2012; Richards 2015). One of the reasons for this may be that the promotion effect of high oxidation state on Cu abundance is confined to a narrow window near the exhaustion of sulfide (mostly at low melting degree), and most parts of Cu trends are identical to each other at high melt fractions, e.g., 20-30 wt. % melting degree as suggested for most arc rocks (Mitchell and Grove 2015; Mallik et al. 2016).

In all, during flux-melting of mantle wedge within subduction zones, temperature is the most important factor controlling the partitioning behavior of Ni, and the temperature distribution of the mantle wedge reflects the influences of convergence rate, slab age, dip, rate of shear heating, vigor and geometry of flow in the mantle wedge and release of latent heat during phase change, and dehydration of the slab (Stern 2002; Simon 2003; Kincaid and Griffiths 2003; Peacock et al. 2005; van Keken et al. 2008; Leng and Mao 2015). Slow convergence rate, young lithosphere and low subduction angle lead to relatively high temperature in the subduction system (Leng and Mao 2015), increasing the Ni abundance in melt. If the dehydration of slab is weak and pre-eruptive water contents are low, or at slab windows, the partial melting occurs at high temperature, similar to the decompression melting in mid-ocean ridges. On the other hand, the melting in cooler subduction zones is usually triggered and enhanced by continuous addition of slab-derived fluids or melts, resulting in a relative low Ni content in the melt. In contrast, although the Cu behavior can be influenced by temperature, S and Cu enrichment, depletion of mantle and oxygen fugacity, showing notable increases in low-degree oxidized melts over all others, the Cu concentrations of most arc magmas are expected to fall in the range from 50 to 100 ppm, which is sufficient for the generation of large porphyry deposits within reasonable magma volumes (Cline and Bodnar 1991; Richards 2015).

6. Implications

1. There is a close relationship between the geodynamic environment of partial melting and ore-potential of mantle-derived magma, which will be of significance for

the delineation of the Ni-Cu exploration target areas at the regional scale. For magmatic sulfide deposits, a thick lithosphere (high pressure) with a hot plume tends to generate melts with higher MgO and Ni contents, whereas there is no clear correlation between magma fertility for porphyry Cu deposits and the detailed aspects of the melting process above subduction zones.

2. In this regard, the comprehensive results can be used as reference values for the MgO content and ore potential of primary melt. If the tectonic setting, thermal state and H_2O abundance of source mantle can be presumed *a priori* for given mineralized magmatic suite, these expectations can be compared with the observed outputs from the system to provide a better understanding of the complex processes that may have occurred in transit through the crust, e.g., assimilation, sulfide segregation, magma evolution and transport, because the characteristics of inflow and outflow magmas have been effectively outlined.

3. This forward model sheds new light on some contentious issues for the genesis of magmatic sulfide deposits; we suggest that the SCLM may play no active role for ore potential of mixed magma during plume-lithosphere interactions and that addition of vast amounts of water released from delaminating material, while potentially generating extensive magmatism, is unlikely to produce magmas highly fertile for the generation of Ni deposits.

4. Our results show that efforts to decipher the NiO content of olivine phenocrysts in basalts strictly in terms of lithospheric thickness (e.g., Matzen et al. 2013, 2017a, b; Niu et al. 2011) must be applied in full consideration of complicating

factors including partial melting mechanisms, last equilibration pressures (e.g., lithospheric thicknesses for plumes) and thermal states of source (e.g., potential temperatures), besides the possible presence of olivine-free pyroxenite mantle in source (Sobolev et al. 2005, 2007).

5. By using completely independent parameterizations for the deportment of Ni in systems containing silicate melt, sulfide melt, and olivine, we have duplicated experimental results and also shown that existing parameterizations of Ni partitioning between sulfide melt and olivine are inconsistent with what is known about Ni partitioning between the more thoroughly understood sulfide melt and silicate melt or olivine and silicate melt systems. The results open a path to improved understanding of olivine-BMS equilibria in mantle peridotite, and further make it easier to distinguish between diverse BMS generations for in situ analyses of Re-Os isotope to trace the evolution of SCLM.

Acknowledgments

We are grateful for the help of Mark Ghiorso and Paul Asimow for instruction on alphaMELTS, especially for the flux melting model. This work is funded by the National Key Research & Development Program of China (2017YFC0601306 and 2017YFC0601204), and a visiting scholar grant provided by the Chinese Scholarship Council. Special thanks go to Alexey Ariskin and an anonymous reviewer for their very useful and constructive comments and to the journal editors, Ekaterina Kiseeva and Keith Putirka for their assistance.

References

Arai, S., and Ishimaru, S. (2008) Insights into petrological characteristics of the lithosphere of mantle wedge beneath arcs through peridotite xenoliths: a review. Journal of Petrology, 49, 665-695.

Ariskin, A.A., Danyushevsky, L.V., Bychkov, K.A., McNeill, A.W., Barmina, G.S., and Nikolaev, G.S. (2013) Modeling solubility of Fe-Ni sulfide in basaltic magmas: the effect of nickel. Economic Geology 108, 1983-2003.

Arndt, N. (2013) The lithospheric mantle plays no active role in the formation of orthomagmatic ore deposits. Economic Geology, 108, 1953-1970.

Arndt, N.T., Lesher, C.M., Czamanske, G.K., Arndt, N.T., Lesher, C.M., and Czamanske, G.K. (2005) Mantle-derived magmas and magmatic Ni-Cu-(PGE) deposits. Economic Geology 100th Aniversary volume, 5-24.

Asimow, P.D. (1997) A thermodynamic model of adiabatic melting of the mantle, 370 p. Ph.D. thesis, Callifonia Institute of Technology.

Asimow, P. D. (2004) The significance of multiple saturation points in the context of polybaric near-fractional melting. Journal of Petrology, 45, 2349-2367.

Asimow, P.D., and Langmuir, C.H. (2003) The importance of water to oceanic mantle melting regimes. Nature, 421, 815-820.

Asimow, P.D., Hirschmann, M.M., and Stolper, E.M. (2001) Calculation of peridotite partial melting from thermodynamic models of minerals and melts, IV. adiabatic decompression and the composition and mean properties of Mid-ocean Ridge Basalts. Journal of Petrology, 42, 963-998.

Asimow, P.D., Dixon, J.E., and Langmuir, C.H. (2004) A hydrous melting and fractionation model for mid-ocean ridge basalts: Application to the Mid-Atlantic Ridge near the Azores. Geochemistry, Geophysics, Geosystems, 5. doi:10.1029/2003GC000568

Aubaud, C. (2004) Hydrogen partition coefficients between nominally anhydrous minerals and basaltic melts. Geophysical Research Letters, 31. Doi: 10.1029/2004GL021341.

Aulbach, S., Mungall, J.E. and Pearson, D.G. (2016) Distribution and processing of highly siderophile elements in cratonic mantle lithosphere. Reviews in Mineralogy and Geochemistry, 81, 239-304.

Baker, M.B., Hirschmann, M.M., Ghiorso, M.S., and Stolper, E.M. (1995) Compositions of near-solidus peridotite melts from experiments and thermodynamic calculations. Nature, 375, 308-311.

Barnes, S.J., and Lightfoot, P.C. (2005) Formation of magmatic nickel sulfide ore deposits and processes affecting their copper and platinum group element contents. Economic Geology, 100, 179-213.

Barnes, S.J., and Robertson, J.C. (2018) Time scales and length scales in magma flow pathways and the origin of magmatic Ni-Cu-PGE ore deposits. Geoscience Frontiers, doi:10.1016/j.gsf.2018.02.006.

Barnes, S.J., Maier, W.D., and Curl, E.A. (2007) Composition of the marginal rocks and sills of the Rustenburg Layered Suite, Bushveld Complex, South Africa: Implications for the formation of the Platinum-group element deposits. Economic Geology, 105, 1491-1511.

Barnes, S.J., Godel, B., Gürer, D., Brenan, J.M., Robertson, J., and Paterson D. (2013) Sulfide-olivine Fe-Ni exchange and the origin of anomalougly Ni rich magmatic sulfides. Economic Geology, 108, 1971-1982.

Barnes, S.J., Cruden, A.R., Arndt, N., and Saumur, B.M. (2016) The mineral system approach applied to magmatic Ni-Cu-PGE sulphide deposits. Ore Geology Reviews, 76, 296-316.

Beattie, P., Ford, C., and Russell, D. (1991) Partition coefficients for olivine-melt and orthopyroxene-melt systems. Contributions to Mineralogy and Petrology, 109, 212-224.

Begg, G.C., Hronsky, J.A.M., Arndt, N.T., Griffin, W.L., O'Reilly, S.Y., and Hayward, N. (2010) Lithospheric, cratonic, and geodynamic setting of Ni-Cu-PGE sulfide deposits. Economic Geology, 105, 1057-1070.

Bell, D.R., and Rossman, G.R. (1992) Water in earth's mantle the role of nominally anhydrous minerals. Science, 255, 1391-1397.

Berry, A.J., Stewart, G.A., O'Neill, H.S.C., Mallmann, G., Mosselmans, J.F.W., (2018) A re-assessment of the oxidation state of iron in MORB glasses. Earth and Planetary Science Letters, 483, 114-123.

Bochrath, C., Ballhaus, C., and Holzheid, A. (2004) Fractionation of platinum-group elements during mantle melting. Science, 305, 1951-1953.

Bolfancasanova, N. (2005) Water in the Earth's mantle. Mineralogical Magazine, 69, 229-258.

Borisov, A., and Danyushevsky, L. (2011) The effect of silica contents on Pd, Pt and Rh solubilites in silicate melts: an experimental study. European Journal of Mineralogy, 23, 355-367.

Borisov, A., and Palme, H. (1997) Experimental determination of the solubility of platinum in silicate melts. Geochimica et Cosmochimica Acta, 125, 265-289.

Botcharnikov, R.E., Holtz, F., Mungall, J.E., Beermann, O., Linnen R.L., and Garbe-Schönberg, D. (2013) Behavior of gold in a magma at sulfide-sulfate transition: Revisited. American Mineralogist, 98, 1459-1464.

Brenan, J.M. (2003) Effects of fO_2, fS_2, temperature, and melt composition on Fe-Ni exchange between olivine and sulfide liquid: Implications fro natural olivine-sulfide assemblages. Geochimica et Cosmochimica Acta, 67, 2663-2681.

Burov, E., Guillou-Frottier, L., d'Acremont, E., Le Pourhiet, L., and Cloetingh, S. (2007) Plume head-lithosphere interactions near intra-continental plate boundaries. Tectonophysics, 434, 15-38.

Canil, D. (1999) The Ni-in-garnet geothermometer: calibration at natural abundances. Contributions to Mineralogy and Petrology, 136, 240-246.

Cline, J.S., and Bodnar, R.J. (1991) Can economic porphyry copper mineralization be generated by a typical calc-alkaline melt? Journal of Geophysical Research, 96, 8113-8126.

Cole, J.W., Graham, I.J., and Gibson, I.L. (1990) Magmatic evolution of late Cenozoic volcanic rocks of the Lau Ridge, Fiji. Contributions to Mineralogy and Petrology, 104, 540-554.

Condie, K.C. (2001) Mantle plumes and their record in earth history. Cambridge Univ. Press, New York.

Cottrell, E., Kelley, K. A., (2011) The oxidation of Fe in MORB glasses and the oxygen fugacity of the upper mantle. Earth and Planetary Science Letters, 305, 270-282.

d'Acremont, E., Leroy, S., and Burov, E. B. (2003) Numerical modelling of a mantle plume: the plume head–lithosphere interaction in the formation of an oceanic large igneous province. Earth and Planetary Science Letters, 206, 379-396.

De Hoog, J.C.M., Mason, P.R.D., and Bergen, M.J.V. (2001) Sulfur and chalcophile elements in subduction zones: constraints from a laser ablation ICP-MS study of melt inclusions from Galunggung Volcano, Indonesia. Geochimica et Cosmochimica Acta, 65, 3147-3164.

Dessai, A.G., Markwick, A., Vaselli, O., and Downes, H. (2004) Granulite and pyroxenite xenoliths from the Deccan Trap: insight into the nature and composition of the lower lithosphere beneath cratonic India. Lithos, 78, 263-290.

Ding, S., and Dasgupta, R. (2017) The fate of sulfide during decompression melting of peridotite – implications for sulfur inventory of the MORB-source depleted upper mantle. Earth and Planetary Science Letters, 459, 183-195.

Dixon, J.E., Dixon, T.H., Bell, D.R., and Malservisi, R. (2004) Lateral variation in upper mantle viscosity: role of water. Earth and Planetary Science Letters, 222, 451-467.

Doucet, L.S., Peslier, A.H., Ionov, D.A., Brandon, A.D., Golovin, A.V., Goncharov, A.G., and Ashchepkov, I.V. (2014) High water contents in the Siberian cratonic mantle linked to metasomatism: an FTIR study of Udachnaya peridotite xenoliths. Geochimica et Cosmochimica Acta, 137, 159-187.

Elkins-Tanton, L.T. (2005) Continental magmatism caused by lithospheric delamination. In G.R. Fouler, D.L. Anderson, J.H. Natland, and D.C. Presnall, Ed., Melting anomalies: their nature and origin. Geological Society of America Special Papers 388, 449-461.

Elkins-Tanton, L.T. (2007) Continental magmatism, volatile recycling, and a heterogeneous mantle caused by lithospheric gravitational instabilities. Journal of Geophysical Research: Solid Earth, 112, 485-493.

Elkins-Tanton, L.T., Grove, T.L., and Donnellynolan, J. (2001) Hot, shallow mantle melting under the Cascades volcanic arc. Geology, 29, 631.

Ernst, R.E. (2014) Large Igneous Provinces, 653 p. Cambridge Univ. Press, Cambridge, United Kingdom.

Farnetani, C.G., and Richards, M.A. (1994) Numerical investigations of the mantle plume initiation model for flood basalt events. Journal of Geophysical Research: Solid Earth, 99, 13813-13833.

Fellows, S.A., and Canil, D. (2012) Experimental study of the partitioning of Cu during partial melting of Earth's mantle. Earth and Planetary Science Letters, 337, 133-143.

Foley, S.F. (2010) A reappraisal of redox melting in the earth's mantle as a function of tectonic setting and time. Journal of Petrology, 52, 1363-1391.

Fortin, M. A., Riddle, J., Desjardins-Langlais, Y., Baker, D. R., (2015) The effect of water on the sulfur concentration at sulfide saturation (SCSS) in natural melts. Geochimica et Cosmochimica Acta, 160, 100-116.

Frost, D.J., and McCammon, C.A. (2008) The redox state of Earth’s mantle. Annual Review of Earth and Planetary Science, 36, 389-420.

Gaetani, G.A., and Grove, T.L. (1997) Partitioning of moderately siderophile elements among olivine, silicate melt, and sulfide melt: constraints on core formation in the Earth and Mars. Geochimica et Cosmochimica Acta, 61, 1829-1846.

Garfunkel, Z. (2008) Formation of continental flood volcanism — the perspective of setting of melting. Lithos, 100, 49-65.

Ghiorso, M.S., and Sack, R.O. (1995) Chemical mass transfer in magmatic processes IV. A revised and internally consistent thermodynamic model for the interpolation and extrapolation of liquid-solid equilibria in magmatic systems at elevated temperatures and pressures. Contributions to Mineralogy and Petrology, 119, 197-212.

Ghiorso, M.S., Hirschmann, M.M, Reiners, P.W., and Iii, V.C.K. (2002) The pMELTS: a revision of MELTS for improved calculation of phase relations and major element partitioning related to partial melting of the mantle to 3 GPa. Geochemistry, Geophysics, Geosystems, 3, 1–35.

Gibson, S.A., Thompson, R.N., and Day, J.A. (2006) Timescales and mechanisms of plume-lithosphere interactions: 40Ar/ 39Ar geochronology and geochemistry of alkaline igneous rocks from the Paraná-Etendeka large igneous province. Earth and Planetary Science Letters, 251, 1-17.

Gorczyk, W., Mole, D.R., and Barnes, S.J. (2017) Plume-lithosphere interaction at craton margins throughout Earth history. Tectonophysics. http://dx.doi.org/10.1016/j.tecto.2017.04.002

Greene, A.R., Scoates, J.S., and Weis, D. (2008) Wrangellia flood basalts in Alaska: a record of plume-lithosphere interaction in a Late Triassic accreted oceanic plateau. Geochemistry, Geophysics, Geosystems, 9, 178-196.

Griffin, W.L., O'Reilly, S.Y., Ryan, C.G., Gaul, O., and Ionov, D.A. (1998) Secular variation in the composition of subcontinental lithospheric mantle: geophysical and geodynamic implications. InJ. Braun, J. Dooley, B. Goleby, R. Hilst, and C. Klootwijk, Ed., Structure and evolution of the Australia continent. American Geophysical Union, Geodynamics Series 26, 1-26.

Griffin, W.L., Ryan, C.G., Kaminsky, F.V., O'Reilly, S.Y., Natapov, L.M., Win, T.T., Kinny, P.D., and Ilupin, I.P. (1999) The Siberian lithosphere traverse: mantle terranes and the assembly of the Siberian Craton. Tectonophysics, 310, 1-35.

Griffin, W.L., O'Reilly, S.Y., Afonso, J.C., and Begg, G.C. (2009) The Composition and Evolution of Lithospheric Mantle: a Re-evaluation and its Tectonic Implications. Journal of Petrology, 50, 1185-1204.

Griffin, W.L., Begg, G.C., and O'Reilly, S.Y. (2013) Continental-root control on the genesis of magmatic ore deposits. Nature Geoscience, 6, 905-910.

Grove, T.L., Till, C.B., and Krawczynski, M.J. (2012) The role of H_2O in subduction zone magmatism. Annual Review of Earth and Planetary Sciences, 40, 413-439.

Guo, J.F., Griffin, W.L., and O'Reilly, S.Y. (1999) Geochemistry and origin of sulphide minerals in mantle xenoliths: Qilin, Southeastern China. Journal of Petrology, 40, 1125-1149.

Hart, S.R., and Davis, K.E. (1978) Nickel partitionging between olivine and silicate melt. Earth and Planetary Science Letters, 40, 203-219.

Harvey, J., Gannoun, A., Burton, K.W., Schiano, P., Rogers, N.W., and Alard, O. (2010) Unravelling the effects of melt depletion and secondary infiltration on mantle Re-Os isotopes beneath the French Massif Central. Geochimica et Cosmochimica Acta, 74, 293-320.

Harvey, J., Warren, J.M., and Shirey, S.B. (2016) Mantle sulfides and their role in Re-Os and Pb isotope geochronology. Reviews in Mineralogy and Geochemistry, 81, 579-649.

Hermann, J., and Spandler, C. J. (2008) Sediment melts at sub-arc depths: an experimental study. Journal of Petrology, 49, 717-740.

Herzberg, C., and O'Hara, M.J. (2002) Plume-associated ultramafic magmas of Phanerozoic age. Journal of Petrology, 43, 1857-1883.

Herzberg, C., and Asimow, P.D. (2008) Petrology of some oceanic island basalts: PRIMELT2.XLS software for primary magma calculation. Geochemistry, Geophysics, Geosystems, 9, doi:10.1029/2008GC002057

Herzberg, C., and Gazel, E. (2009) Petrological evidence for secular cooling in mantle plumes. Nature, 458, 619-622.

Herzberg, C., and Asimow, P.D. (2015) PRIMELT3 MEGA.XLSM software for primary magma calculation: Peridotite primary magma MgO contents from the liquidus to the solidus. Geochemistry, Geophysics, Geosystems, 16, 563-578.

Herzberg, C., Asimow, P.D., Arndt, N., Niu, Y., Lesher, C.M., Fitton, J.G., Cheadle, M.J., and Saunders, A.D (2007) Temperatures in ambient mantle and plumes: Constraints from basalts, picrites, and komatiites. Geochemistry, Geophysics, Geosystems, 8. doi:10.1029/2006GC001390.

Herzberg, C., Asimow, P.D., Ionov, D.A., Vidito, C., Jackson, M.G., and Geist, D. (2013) Nickel and helium evidence for melt above the core-mantle boundary. Nature, 493, 393-398.

Herzberg, C., Vidito, C., and Starkey, N.A. (2016) Nickel-cobalt contents of olivine record origins of mantle peridotite and related rocks. American Mineralogist, 101, 1952-1966.

Hirose, K., and Kushiro, I. (1993) Partial melting of dry peridotites at high pressures: Determination of compositions of melts segregated from peridotite using aggregates of diamond. Earth and Planetary Science Letters, 114, 477-489.

Hirose, K., and Kawamoto, T. (1995) Hydrous partial melting of lherzolite at 1 GPa: The effect of H_2O on the genesis of basaltic magmas. Earth and Planetary Science Letters, 133, 463-473.

Hirschmann, M.M. (2006) Water, melting and the deep earth H_2O cycle. Annual Review of Earth and Planetary Sciences, 34, 629-653.

Hirth, G., and Kohlstedt, D.L. (1996) Water in the oceanic upper mantle: implications for rheology, melt extraction and the evolution of the lithosphere. Earth and Planetary Science Letters, 144, 93-108.

Holzheid, A., and Lodders, K. (2001) Solubility of copper in silicate melts as a function of oxygen and sulfur fugacities, temperature and silicate composition. Geochimica et Cosmochimica Acta, 65, 1933-1951.

Hui, H., Peslier, A.H., Rudnick, R. L., Simonetti, A., and Neal, C.R. (2015) Plume-cratonic lithosphere interaction recorded by water and other trace elements in peridotite xenoliths from the Labait volcano, Tanzania. Geochemistry, Geophysics, Geosystems, 16, 1687-1710.

Humphreys, E. R., and Niu, Y. (2009) On the composition of ocean island basalts (OIB): the effects of lithospheric thickness variation and mantle metasomatism. Lithos, 112, 118-136.

Ingle, S., Weis, D., Scoates, J.S., and Frey, F. A. (2002) Relationship between the early Kerguelen plume and continental flood basalts of the paleo-Eastern Gondwanan margins. Earth and Planetary Science Letters, 75, 35-50.

Jaques, A.L., and Green, D.H. (1980) Anhydrous melting of peridotite at 0–15 Kb pressure and the genesis of tholeiitic basalts. Contributions to Mineralogy and Petrology, 73, 287-310.

Jégo, S., and Dasgupta, R. (2013) Fluid-present melting of sulfide-bearing ocean-crust: Experimental constraints on the transport of sulfur from subducting slab to mantle wedge. Geochimica et Cosmochimica Acta, 110, 106-134.

Jégo, S., and Dasgupta, R. (2014) The fate of sulfur during fluid-present melting of subducting basaltic crust as variable oxygen fugacity. Journal of Petrology, 55, 1019-1050.

Jenner, F.E., O'Neill, H.S.C., Arculus, R.J., and Mavrogenes, J.A. (2010) The magnetite crisis in the evolution of arc-related magmas and the initial concentration of Au, Ag and Cu. Journal of Petrology, 51, 2445-2464.

Jennings, E.S., and Holland, T.J.B. (2015) A simple thermodynamic model for melting of peridotite in the system NCFMASOCr. Journal of Petrology, 56, 869-892.

Jowitt, S.M., and Ernst, R.E. (2013) Geochemical assessment of the metallogenic potential of Proterozoic LIPs of Canada. Lithos, 174, 291-307.

Jugo, P.J., Wilke, M., and Botcharnikov, R.E. (2010) Sulfur K-edge XANES analysis of natural and synthetic basaltic glasses: implications for S speciation and S content as function of oxygen fugacity. Geochimica et Cosmochimica Acta, 74, 5926-5938.

Karmalkar, N.R., Duraiswami, R.A., Rao, N.V.C., and Paul, D.K. (2009) Mantle-derived mafic-ultramafic xenoliths and the nature of Indian sub-continental lithosphere. Journal of the Geological Society of India, 73, 657-679.

Katz, R.F., Spiegelman, M., and Langmuir, C. H. (2003) A new parameterization of hydrous mantle melting. Geochemistry, Geophysics, Geosystems, 4. Doi:10.1029/2002GC000433

Kelley, K.A., and Cottrell, E. (2009) Water and the oxidation state of subduction zone magmas. Science, 325, 605-607.

Kerr, A.C., and Mahoney, J.J. (2007) Oceanic plateaus: problematic plumes, potential paradigms. Chemical Geology, 241, 332-353.

Kessel, R., Schmidt, M.W., Ulmer, P., and Pettke, T. (2005a) Trace element signature of subduction-zone fluids, melts and supercritical liquids at 120-180 km depth. Nature, 437, 724-727.

Kessel, R., Ulmer, P., Pettke, T., Schmidt, M.W., and Thompson, A.B. (2005b) The water–basalt system at 4 to 6 GPa: phase relations and second critical endpoint in a K-free eclogite at 700 to 1400 °C. Earth and Planetary Science Letters, 237, 873-892.

Kimura, J.I., and Kawabata, H. (2014) Trace element mass balance in hydrous adiabatic mantle melting: the hydrous adiabatic mantle melting simulator version 1 (HAMMS1). Geochemistry, Geophysics, Geosystems, 15, 2467-2493.

Kincaid, C., and Griffiths, R.W. (2003) Laboratory models of the thermal evolution of the mantle during rollback subduction. Nature, 425, 58-62.

Kiseeva, E.S., and Wood, B.J. (2013) A simple model for chalcophile element partitioning between sulphide and silicate liquids with geochemical applications. Earth and Planetary Science Letters, 383, 68-81.

Kiseeva, E.S., and Wood, B.J. (2015) The effects of composition and temperature on chalcophile and lithophile element partitioning into magmatic sulphides. Earth and Planetary Science Letters, 424, 280-294.

Kiseeva, E.S., Fonseca, R.O.C., Smythe, D.J. (2017) Chalcophile elements and sulfides in the upper mantle. Elements, 13, 111-116.

Kohn, S.C. (2006) The partitioning of water between nominally anhydrous minerals and silicate melts. Reviews in Mineralogy and Geochemistry, 62, 231-241.

Koptev, A., Calais, E., Burov, E., Leroy, S., and Gerya,T. (2015) Dual continental rift systems generated by plume-lithosphere interaction. Nature Geoscience, 8, 388-392.

Korenaga, J. (2005) Why did not the Ontong Java Plateau form subaerially? Earth and Planetary Science Letters, 234, 385-399.

Langmuir, C.H., Klein, E.M., and Plank, T. (1993) Petrological systematics of Mid-Ocean Ridge Basalts: constraints on melt generation beneath ocean ridges. In: Morgan, J. P., Blackman, D. K. and Plank T. (ed.) Mantle flow and melt generation at Mid-ocean ridges. American Geophysical Union., Washington, 183-280. doi:10.1029/GM071p0183

Laubier, M., Grove, T.L., and Langmuir, C.H. (2014) Trace element mineral/melt partitioning for basaltic and basaltic andesitic melts: an experimental and laser

ICP-MS study with application to the oxidation state of mantle source regions. Earth and Planetary Science Letters, 392, 265-278.

Lee, C.T.A., Luffi, P., Plank, T., Dalton, H., and Leeman, W.P. (2009) Constraints on the depths and temperatures of basaltic magma generation on Earth and other terrestrial planets using new thermobarometers for mafic magmas. Earth and Planetary Science Letters, 279, 20-33.

Lee, C.T.A., Luffi, P., Chin, E.J., Bouchet, R., Dasgupta, R., Morton, D.M., Le Roux, V., Yin, Q.Z., and Jin, D. (2012) Copper systematics in arc magmas and implications for crust-mantle differentiation. Science, 336, 64-68.

Leng, W., and Mao, W. (2015) Geodynamic modeling of thermal structure of subduction zones. Science China Earth Sciences, 58, 1070-1083.

Le Roux, V., Dasgupta, R. and Lee, C.T. (2011) Mineralogical heterogeneities in the Earth's mantle: constraints from Mn, Co, Ni and Zn partitioning during partial melting. Earth and Planetary Science Letters, 307, 395-408.

Le Roux, V., Dasgupta, R., and Lee, C.T. (2015) Recommended mineral-melt partition coefficients for FRTEs (Cu), Ga and Ge during mantle melting. American Mineralogist, 100, 2533-2544.

Lesne, P., Scaillet, B., and Pichavant, M. (2015) The solubility of sulfur in hydrous basaltic melts. Chemical Geology, 418, 104-116.

Li, C., and Ripley, E.M. (2009) Sulfur contents at sulfide-liquid or anhydrite saturation in silicate melts: empirical equations and example applications. Economic Geology, 104, 405-412.

Li, C., and Ripley, E.M. (2010) The relative effects of composition and temperature on olivine-liquid Ni partitioning: Statistical deconvolution and implications for petrologic modeling. Chemical Geology, 275, 99-104.

Li, C., Tao, Y., Qi, L., and Ripley, E.M. (2012) Controls on PGE fractionation in the Emeishan picrites and basalts: constraints from integrated lithophile–siderophile elements and Sr–Nd isotopes. Geochimica et Cosmochimica Acta, 90, 12-32.

Li, Y., and Audétat, A. (2013) Partitioning of V, Mn, Co, Ni, Cu, Zn, As, Mo, Ag, Sn, Sb, W, Au, Pb and Bi between sulfide phases and hydrous basanite melt at upper mantle conditions. Earth and Planetary Science Letters, 355-356, 327-340.

Lightfoot, P.C., and Keays, R.R. (2005) Siderophile and chalcophile metal variations in flood basalts from the Siberian Trap, Noril'sk region: implications for the origin of the Ni-Cu-PGE sulfide ores. Economic Geology, 100, 439-462.

Lightfoot, P.C., Keays, R.R., Evans-Lamswood, D., and Wheeler, R. (2012) S saturation history of Nain Plutonic Suite mafic intrusions: origin of the Voisey's Bay Ni–Cu–Co sulfide deposit, Labrador, Canada. Mineralium Deposita, 47, 23-50.

Liu, J., Xia, Q.K., Kuritani, T., Hanski, E., and Yu, H.R. (2017) Mantle hydration and the role of water in the generation of large igneous provinces. Nature Communications. Doi:10.1038/s41467-017-01940-3

Liu, X., Xiong, X., Audétat, A., Li, Y., Song, M., Li, L., Sun, W., and Ding, X. (2014)

Partitioning of copper between olivine, orthopyroxene, clinopyroxene, spinel, garnet and silicate melts at upper mantle conditions. Geochimica et Cosmochimica Acta, 125, 1-22.

Liu, Y., Samaha, N.T., and Baker, D.R. (2007) Sulfur concentration at sulfide saturation (SCSS) in magmatic silicate melts. Geochimica et Cosmochimica Acta, 71, 1783-1799.

Lorand, J.P., and Luguet, A. (2016) Chalcophile and siderophile elements in mantle rocks: trace elements controlled by trace minerals. Reviews in Mineralogy and Geochemistry, 81, 441-488.

Lustrino, M. (2005) How the delamination and detachment of lower crust can influence basaltic magmatism. Earth-Science Reviews, 72, 21-38.

Lynton, S.J., Candela, P.A., and Piccoli, P.M. (1993) An experimental study of the partitioning of copper between pyrrhotite and a high silica rhyolitic melt. Economic Geology, 88, 901-915.

Mallik, A., Dasgupta, R., Tsuno, K., and Nelson, J. (2016) Effects of water, depth and temperature on partial melting of mantle-wedge fluxed by hydrous sediment-melt in subduction zones. Geochimica et Cosmochimica Acta, 195, 226-243.

Manglik, A., and Christensen, U.R. (2006) Effect of lithospheric root on decompression melting in plume-lithosphere interaction models. Geophysical Journal International, 164, 259-270.

Mao, Y.J. Qin, K.Z., Li, C., and Tang, D.M. (2014) A modified genetic model for the Huangshandong magmatic sulfide deposit in the Central Asian Orogenic Belt, Xinjiang, western China. Mineralium Deposita, 50, 65-82.

Marcantonio, F., Reisberg, L., Zindler, A., Wyman, D., and Hulbert, L. (1994) An isotopic study of the Ni-Cu-PGE-rich Wellgreen intrusion of the Wrangellia Terrane: evidence for hydrothermal mobilization of rhenium and osmium. Geochimica et Cosmochimica Acta, 58, 1007-1018.

Matzen, A.K., Baker, M.B., Beckett, J.R., and Stolper, E.M. (2013) The temperature and pressure dependence of nickel partitioning between olivine and silicate melt. Journal of Petrology, 54, 2521-2545.

Matzen, A.K., Baker, M.B., Beckett, J.R., Wood, B.J., and Stolper, E.M. (2017a) The effect of liquid composition on the partitioning of Ni between olivine and silicate melt. Contributions to Mineralogy and Petrology, 172, 3. doi:10.1007/s00410-016-1319-8

Matzen, A.K., Wood, B.J., Baker, M.B., and Stolper, E.M. (2017b). The roles of pyroxenite and peridotite in the mantle sources of oceanic basalts. Nature Geosicence, 10, 530-535.

Mavrogenes, J., and O'Neil, H.S.C. (1999) The relative effects of pressure, temperature and oxygen fugacity on the solubility of sulfide in mafic magmas. Geochimica et Cosmochimica Acta, 63, 1173-1180.

McDonough, W.F., and Sun, S.S (1995) The composition of the Earth. Chemical Geology, 120, 223-253.

McKenzie, D., and Bickle, M.J. (1988) The volume and composition of melt generated by extension of the lithosphere. Journal of Petrology, 29, 625-679.

Michael, P.J. (2000) Implications for magmatic processes at Ontong Java Plateau from volatile and major element contents of Cretaceous basalt glasses. Geochemistry, Geophysics, Geosystems, 1. Doi:10.1029/1999GC000025

Mitchell, A.L., and Grove, T.L. (2015) Melting the hydrous, subarc mantle: the origin of primitive andesites. Contributions to Mineralogy and Petrology, 170, 23.

Moretti, R., and Baker, D.R. (2008) Modeling the interplay of fO_2 and fS_2 along the FeS-silicate melt equilibrium. Chemical Geology, 256, 286-298.

Mungall, J.E. (2002) Roasting the mantle: slab melting and the genesis of major Au and Au-rich Cu deposits. Geology, 30, 915-918.

Mungall, J.E. (2014) Geochemistry of magmatic ore deposits. Treatise on Geochemistry: Geochemistry of Mineral deposits (Elsevier, Amsterdam), 2nd Ed Vol 13, 195-218.

Mungall, J.E., and Brenan, J.M. (2014) Partitioning of platinum-group elements and Au between sulfide liquid and basalt and the origins of mantle-crust fractionation of the chalcophile elements. Geochimica et Cosmochimica Acta, 125, 265-289.

Mungall, J.E., Andrews, D.R.A., Cabri, L.J., Sylvester, P.J., and Tubrett, M. (2005) Partitioning of Cu, Ni, Au, and platinum-group elements between monosulfide solid solution and sulfide melt under controlled oxygen and sulfur fugacities. Geochimica et Cosmochimica Acta, 69, 4349-4360.

Mungall, J.E., Hanley, J.J., Arndt, N.T., and Debecdelievre, A. (2006) Evidence from meimechites and other low-degree mantle melts for redox controls on mantle-crust fractionation of platinum-group elements. Proceeding of the National Academy of Sciences, 103, 12695-12700.

Naldrett, A.J. (2010) From the mantle to the bank: the life of a Ni-Cu-(PGE) sulfide deposit. South African Journal of Geology, 113, 1-32.

Naldrett, A.J. (2011) Fundamentals of magmatic sulfide deposits. In C. Li, and E.M. Ripley, Ed., Magmatic Ni-Cu and PGE deposits: geology, geochemistry and genesis: reviews in economic geology, volume 17. Society of Economic Geologists, Denver., 1-50.

Nielsen, S.G., Shimizu, N., Lee, C.T., and Behn, M.D. (2014) Chalcophile behavior of thallium during MORB melting and implications for the sulfur content of the mantle. Geochemistry, Geophysics, Geosystems, 15, 4905-4919.

Niu, Y., and O'Hara, M.J. (2008) Global correlations of ocean ridge basalt chemistry with axial depth: a new perspective. Journal of Petrology, 49, 633-664.

Niu, Y., Wilson, M., Humphreys, E.R., and O'Hara, M.J. (2011) The origin of intra-plate ocean island basalts (OIB): the lid effect and its geodynamic implications. Journal of Petrology, 52, 1443-1468.

O'Neill, H.S.C. (1991) The origin of the Moon and the early of the Earth – a chemical model. Part 2: the Earth. Geochimica et Cosmochimica Acta, 55, 1159-1172.

Oyarzun, R., Márquez, A., Lillo, J., López, I., and Rivera, S. (2001) Giant versus small porphyry copper deposits of Cenozoic age in northern Chile: adakitic versus normal calc-alkaline magmatism. Mineralium Deposita, 36, 794-798.

Peacock, S., van Keken, P.E., Holloway, S.D., Hacker, B.R., Abers, G.A., and Fergason, R.L. (2005) Thermal structure of the Costa Rica – Nicaragua subduction zone. Physics of the Earth and Planetary Interiors, 149, 187-200.

Peslier, A.H (2010) A review of water contents of nominally anhydrous natural minerals in the mantles of Earth, Mars and the Moon. Journal of Volcanology and Geothermal Research, 197, 239-258.

Peslier, A., and Luhr, J. (2006) Hydrogen loss from olivines in mantle xenoliths from Simcoe (USA) and Mexico: Mafic alkalic magma ascent rates and water budget of the sub-continental lithosphere. Earth and Planetary Science Letters, 242, 302-319.

Peslier, A.H., Luhr J.F., and Post J. (2002) Low water contents in pyroxenes from spinel-peridotites of the oxidized, sub-arc mantle wedge. Earth and Planetary Science Letters, 201, 69-86.

Peslier, A.H., Woodland A.B., Bell D.R., Lazarov M., and Lapen T.J. (2012) Metasomatic control of water contents in the Kaapvaal cratonic mantle. Geochimica et Cosmochimica Acta, 97, 213-246.

Plank, T., and Langmuir, C.H. (1988) An evaluation of the global variations in the major element chemistry of arc basalts. Earth and Planetary Science Letters, 90, 349-370.

Prichard, H.M., Neary, C.R., Fisher, P.C., and O'Hara, M.J. (2008) PGE-rich podiform chromitites in the Al 'Ays ophiolite complex, Saudi Arabia: an example of critical mantle melting to extract and concentrate PGE. Economic Geology, 103, 1507-1529.

Prouteau, G., and Scaillet, B. (2013) Experimental constraints on sulphur behaviour in subduction zones: I mplications for TTG and adakite production and the global sulphur cycle since the Archean. Journal of Petrology, 54, 183-213.

Putirka, K.D. (2005) Mantle potential temperatures at Hawaii, Iceland, and the mid-ocean ridge system, as inferred from olivine phenocrysts: Evidence for thermally driven mantle plumes. Geochemistry, Geophysics, Geosystems, 6. doi:10.1029/2005GC000915

Putirka, K. D. (2016) Rates and styles of planetary cooling on Earth, Moon, Mars, and Vesta, using new models for oxygen fugacity, ferric-ferrous ratios, olivine-liquid Fe-Mg exchange, and mantle potential temperature. American Mineralogist, 101， 819-840.

Putirka, K.D., Perfit, M., Ryerson, F.J., and Jackson, M.G. (2007). Ambient and excess mantle temperatures, olivine thermometry and active vs. passive upwelling. Chemical Geology, 241, 177-206.

Putirka, K.D., Ryerson, F.J., Perfit, M., and Ridley, W.I. (2011) Mineralogy and composition of oceanic mantle. Journal of Petrology, 52, 279-313.

Qin, K.Z., Su, B.X., Sakyi, P.A., Tang, D.M., Li, X.H., Sun, H., Xiao, Q.H., and Liu, P.P. (2011) SIMS Zircon U-Pb geochronology and Sr-Nd isotopes of Ni-Cu bearing mafic-ultramafic intrusions in Eastern Tianshan and Beishan in correlation with flood basalts in Tarim Basin (NW China): constraints on a ca. 280 Ma mantle plume. American Journal of Science, 311(3), 237-260.

Ragozin, A.L., Karimova, A.A., Litasov, K.D., Zedgenizov, D.A., and Shatsky, V.S. (2014) Water content in minerals of mantle xenoliths from the Udachnaya pipe kimberlites (Yakutia). Russian Geology and Geophysics, 55, 428-442.

Révillon, S., Arndt, N.T., Chauvel, C., and Hallot, E. (2000) Geochemical study of ultramafic volcanic and plutonic rocks from Gorgona island, Colombia: the plumbing system of an oceanic plateau. Journal of Petrology, 41, 1127-1153.

Rey, P.F. (2015) The geodynamics of mantle melting. Geology, 43, 367-368.

Ribe, N.M., and Christensen, U.R. (1999) The dynamical origin of Hawaiian volcanism. Earth and Planetary Science Letters, 171, 517-531.

Richards, J.P. (2015) The oxidation state, and sulfur and Cu contents of arc magmas: implications for metallogeny. Lithos, 233, 27-45.

Righter, K., Campbell, A.J., Humayun, M., and Hervig, R.L. (2004) Partitioning of Ru, Rh, Pd, Re, Ir, and Au between Cr-bearing spinel, olivine, pyroxene and silicate melts. Geochimica et Cosmochimica Acta, 68, 867-880.

Ripley, E.M., Brophy, J.G., and Li, C. (2002) Copper solubility in a basaltic melt and sulfide liquid/silicate melt partition coefficients of Cu and Fe. Geochimica et Cosmochimica Acta, 125, 265-289.

Robertson, J.C., Barnes, S.J., and Le Vaillant, M. (2015) Dynamics of magmatic sulphide droplets during transport in silicate melts and implications for magmatic sulphide ore formation. Journal of Petrology, 56, 2445-2472.

Salters, V.J.M., and Stracke, A. (2004) Composition of the depleted mantle. Geochemistry, Geophysics, Geosystems, 5. doi:10.1029/2003GC000597

Sattari, P., Brenan, J.M., Horn, I., and McDonough, W.F. (2002) Experimental constraints on the sulfide- and chromite-silicate melt partitioning behavior of rhenium and the platinum-group elements. Economic Geology, 97, 385-398.

Sciortino, M., Mungall, J.E., and Muinonen J. (2015) Generation of high-Ni sulfide and alloy phases during serpentinzation of dunite in the Dumont Sill, Quebec. Economic Geology, 110, 733-761.

Seitz, H.M., Altherr, R., and Ludwig, T. (1999) Partitioning of transition elements between orthopyroxene and clinopyroxene in peridotitic and websteritic xenoliths: New empirical geothermometers. Geochimica et Cosmochimica Acta, 35, 3967-3982.

Shaw, D.M. (1970). Trace element fractionation during anatexis. Geochimica et Cosmochimica Acta, 34, 237-243.

Shimize, K., Saal, A.E., Myers, C.E., Nagle, A.N., Hauri, E.H., Forsyth, D.W., Kamenetsky, V.S., and Niu, Y. (2016) Two-component mantle melting-mixing model for the generation of mid-ocean ridge basalts: implications for the volatile content of the Pacific upper mantle. Geochimica et Cosmochimica Acta, 176, 44-80.

Simon, M.P. (2003) Thermal structure and metamorphic evolution of subducting slabs. In Inside the Subduction Factory. In J.M. Eiler, Ed., Washington DC: AGU. pp. 7-22.

Smith, P.M., and Asimow, P.D. (2005) Adiabat_1ph: a new public front-end to the MELTS, pMELTS, and pHMELTS models. Geochemistry, Geophysics, Geosystems, 6. doi:10.1029/2004GC000816

Smythe, D.J., Wood, B.J., and Kiseeva, E.S. (2017) The S content of silicate melts at sulfide saturation: New experiments and a model incorporating the effects of sulfide composition. American Mineralogist, 102, 795-803.

Sobolev, A.V., Hofmann, A.W., Sobolev, S.V., and Nikogosian, I.K. (2005) An olivine-free mantle source of Hawaiian shield basalts. Nature, 434, 590-597.

Sobolev, A.V., Hofmann, A.W., Kuzmin, D.V., Yaxley, G.M., Arndt, N.T., Chung, S.L., Danyushevsky, L.V., Elliott, T., Frey, F.A., Garcia, M.O., Gurenko, A.A., Kamenetsky, V.S., Kerr, A.C., Krivolutskaya, N.A., Matvienkov, V.V., Nikogosian, I.K., Rocholl, A., Sigurdsson, I.A., Sushchevskaya, N.M., and Teklay, M. (2007) The amount of recycled crust in sources of mantle-derived melts. Science, 316, 412-417.

Sobolev, A.V., Sobolev, S.V., Kuzmin, D.V., Malitch, K.N., and Petrunin, A.G. (2009) Siberian meimechites: origin and relation to flood basalts and kimberlites. Russian Geology and Geophysics, 50, 999-1033.

Sobolev, A.V., Asafov, E.V., Gurenko, A.A., Arndt, N.T., Batanova, V.G., Portnyagin, M.V., Garbe-Schönberg, D., and Krasheninnikov, S.P. (2016) Komatiites reveal a hydrous Archaean deep-mantle reservoir. Nature, 531, 628-632.

Spandler, C., and Pirard, C. (2013) Element recycling from subducting slabs to arc crust: a review. Lithos, 170-171, 208-223.

Stern, R.J. (2002) Subduction zones. Reviews of Geophysics, 40. doi:10.1029/2001RG000108

Stolper, E., and Newman, S. (1994) The role of water in the petrogenesis of Mariana trough magmas. Earth and Planetary Science Letters, 121, 293-325.

Sun, S.S. (1982) Chemical composition and origin of the Earth's primitive mantle. Geochimica et Cosmochimica Acta, 46, 179-192.

Tatsumi, Y. and Eggins, S. (1995) Subduction zone magmatism, 224 p. Blackwell Science, Cambridge, MA.

Tatsumi, Y., Sakuyama, M., Fukuyama, H., and Kushiro, I. (1983) Generation of arc basalt magmas and thermal structure of the mantle wedge in subduction zones. Journal of Geophysical Research: Solid Earth, 88, 5815–5825.

Thompson, R.N., and Gibson, S.A. (2000) Transient high temperatures in mantle plume heads inferred from magnesian olivines in Phanerozoic picrites. Nature, 407, 502-506.

Till, C.B., Grove, T.L., and Krawczynski, M.J. (2012) A melting model for variably depleted and enriched lherzolite in the plagioclase and spinel stability fields. Journal of Geophysical Research, 117. Doi:10.1029/2011JB009044

Ueki, K., and Iwamori, H. (2013) Thermodynamic model for partial melting of peridotite by system energy minimization. Geochemistry, Geophysics, Geosystems, 14. Doi:10.1029/2012GC004143

Van Keken, P.E., Currie, C.A., King, S.D., Behn, M.D., Cagnioncle, A.M., He, J., Katz, R.F., Lin, S.C., Parmentier, E.M., Speigelman, M., and Wang, K. (2008) A community benchmark for subduction zone modeling. Physics of the Earth and Planetary Interiors, 171, 187-197.

Wallace, P.J. (2002) Volatiles in submarine basaltic glasses from the northern Kerguelen Plateau (ODP Site 1140): implications for source region compositions, magmatic processes, and Plateau subsidence. Journal of Petrology, 43, 1311-1326.

Walter, M.J. (1998) Melting of garnet peridotite and the origin of Komatiite and depleted lithosphere. Journal of Petrology, 39, 29-60.

Wang, K.L., O'Reilly, S.Y., Griffin, W.L., Pearson, N.J., and Zhang, M. (2009) Sulfide in mantle peridotites from Penghu Islands, Taiwan: Melt percolation, PGE fractionation, and the lithospheric evolution of the South China block. Geochimica et Cosmochimica Acta, 73, 4531-4557.

Wang, Z., and Becker, H. (2013) Ratios of S, Se and Te in the silicate Earth require a volatile-rich late veneer. Nature, 499, 328-331.

Wang, Z., and Becker, H. (2015) Abundance of Ag and Cu in mantle peridotites and the implications for the behavior of chalcophile elements in the mantle. Geochimica et Cosmochimica Acta, 160, 209-226.

Weis, D., Frey, F.A., Schlich, R., Schaming, M., Montigny, R., Damasceno, D., Mattielli, N., Nicolaysen, K.E., and Scoates, J.S. (2002) Trace of the Kerguelen mantle plume: evidence from seamounts between the Kerguelen Archipelago and Heard Island, Indian Ocean. Geochemistry, Geophysics, Geosystems, 3, 1-27.

Wilson, J.T. (1963) A possible origin of the Hawaiian Islands. Canadian Journal of Physics, 41, 863-870.

White, W.M. (2007) Geochemistry. John-Hopkins University Press, pp. 273-324.

White, W.M. (2010) Oceanic island basalts and mantle plumes: the geochemical perspective. Annual Review of Earth and Planetary Sciences, 38, 133-160.

Workman, R.K., and Hart, S.R. (2005) Major and trace element composition of the depleted MORB mantle (DMM). Earth and Planetary Science Letters, 231, 53-72.

Xia, Q.K., Hao, Y., Li, P., Deloule, E., Coltorti, M., Dallai, L., Yang, X., and Feng, M. (2010) Low water content of the Cenozoic lithospheric mantle beneath the eastern part of the North China Craton. Journal of Geophysical Research: Solid Earth, 115. doi:10.1029/2009JB006694

Xu, J.H., and Xie, Y.L. (2007) Sulfide-melt inclusions in mantle xenoliths from the Changbaishan district, Jilin province, China. Acta Petrologica Sinica, 23, 117-124.

Yang, X.Z., Xia, Q.K., Deloule, E., Dallai, L., Fan, Q.C., and Feng, M. (2008) Water in minerals of the continental lithospheric mantle and overlying lower crust: A comparative study of peridotite and granulite xenoliths from the North China Craton. Chemical Geology, 256, 33-45.

Zhang, C.C., Sun, W.D., Wang, J.T., Zhang, L.P., Sun, S.J., and Wu, K. (2017) Oxygen fugacity and porphyry mineralization: A zircon perspective of Dexing porphyry Cu deposit, China. Geochimica et Cosmochimica Acta, 206, 343-363.

Zhang, H.L., Cottrell, E., Solheid, P.A., Kelley, K.A., Hirschmann, M.M. (2018)

Determination of $Fe^{3+}/\sum Fe$ of XANES basaltic glass standards by Mössbauer spectroscopy and its application to the oxidation state of iron in MORB. Chemical Geology, 479, 166-175.

Zhang, M., O'Reilly, S.Y., Wang, K.L., Hronsky, J., and Griffin, W.L. (2008) Flood basalts and metallogeny: The lithospheric mantle connection. Earth-Science Reviews, 86, 145-174.

Zhang, Z., and Hirschmann, M.M. (2016) Experimental constraints on mantle sulfide melting up to 8 GPa. American Mineralogist, 101, 181-192.

Figure captions

Fig. 1. Phase diagram of mantle melting (modified from Rey 2015). Primary melts are initially produced at solidus temperatures (blue and red stars). If they are extracted at the onset of melting, they would follow their respective melt adiabat (solid blue and red arrows). For the polybaric continuous melting in mid-ocean ridges, melt is usually extracted with a minor part retained in the residual source. As latent heat escapes with melt, the source cools and follows the solidus during its exhumation (path a-a'). In a mantle plume, the adiabatic upwelling of source keeps following the adiabat (path b-b'). Once the upwelling ceases at the base of lithosphere (b'), magma will be extracted following the melt adiabat (empty red arrow). The water-saturated solidus was predicted by the pHMELTS model (Ghiorso et al. 2002), showing that addition of water can cause melting to begin at a higher pressure under constant potential temperature. The filled blue and red circles mark the potential temperature (T_p) for mantle exhumation (e.g., polybaric continuous melting of DMM) and mantle plume upwelling, respectively.

Fig. 2. Variations of Ni in pooled melts during the polybaric continuous melting of DMM with constant potential temperature (T_p=1350℃), different water contents (0-250 ppm) and fractions of remaining melt (**a**, 0.3 vol.%; **b**, 0.5 vol.%; **c**, 0.7 vol.%). The influence of water abundances (0-250 ppm) on the partitioning behaviors of Cu (**d**), the trends of MgO (**e**) and FeO (**f**) within the aggregated melt at 1350℃ T_p and 0.3 vol. % remaining melt. In addition, the variations of $D_{Ni}^{Ol/melt}$ and $D_{Cu}^{sul/melt}$ within low melting degree (0-3 wt.%) are shown in the schematic inset diagrams in (**e**) and (**f**). The dash lines in (**a**, **b**, **c**, **d**) are the constant pressure lines in these models, and the variations of residual sulfide compositions (Ni and Cu abundances) before complete exhaustion are also provided in (**a**, **b**, **c**). The gray vertical bands in (**a-f**) indicate the reference area in which the residual sulfide has been completely dissolved.

Fig. 3. Influences of different potential temperature on the evolutions of (**a**). Ni, (**b**).

Cu, (**c**). MgO and (**d**). FeO abundances in the pooled melts during the polybaric continuous melting of DMM with 150 ppm H_2O and 1 vol. % remaining melt. The dash lines in (**a-d**) are the constant pressure lines in these models.

Fig. 4. Variations of (**a**, **c**, **e**) Ni and (**b**, **d**, **f**) MgO in the instantaneous, equilibrated melts during the adiabatic melting of primary mantle with different potential temperatures (1500, 1550 and 1600℃) and water contents (0-6000 ppm). Note that these high T_p melting paths begin at 4.0 GPa with some melt already present as described in the text. The dash lines in (**a-f**) mean the constant pressure values. The gray vertical bands in (**a-f**) indicate the reference area in which the residual sulfide has been completely dissolved.

Fig. 5. Partitioning behavior of Cu in the instantaneous, equilibrated melts during adiabatic melting of mantle at (**a**). 1500℃ and (**b**). 1550℃ potential temperatures. The dotted line in (**a**) shows the constant pressure condition (3.9 GPa), and the variations of residual sulfide compositions (Ni and Cu abundances) before complete exhaustion were also provided in (**a**, **b**). The gray vertical bands in (**a**) and (**b**) indicate the reference area in which residual sulfide has been completely dissolved.

Fig. 6. Results of isobaric melting model for SCLM. (**a**). the behaviors of Ni in the isobaric melting of A-, P- and T-SCLMs under constant pressure (3.9 GPa) and water content (50 ppm); (**b**) the trends of Ni in isobaric melting model of T-SCLMs at different pressure (1.5, 2.7 and 3.9 GPa); The gray vertical band in (**b**) indicates the reference area that the residual sulfide has been completely dissolved. The variations of (**c**) MgO and (**d**) Cu in the melt derived from isobaric melting of A-, P- and T-SCLMs at 3.9 GPa, in conjunction with T-SCLMs melting at 1.5 and 2.7 GPa. The dotted lines in (**a-d**) represent the unrealizable parts of isobaric melting as their temperatures exceed the threshold values that assumed as the temperatures of underlying hotter mantle (white dots, T_p=1500℃; black dots, T_p=1550℃; red dots, T_p=1600℃) at the same pressure. Moreover, the variations of residual sulfide

compositions (Ni and Cu abundances) are also exhibited in (**d**). (**e**, **f**). the influences of water addition (0-300 ppm) on the abundances of Ni, Cu in melt and the melt productivity (%/ºC) in isobaric melting model of T-SCLMs at 3.9 GPa. The light blue vertical bands in (**e**) and (**f**) indicate the influences of water addition on the sulfide exhaustions.

Fig. 7. In flux-melting mode, the partitioning behaviors of (**a**) Ni, (**b**) MgO and (**c**) Cu abundances in the aggregated melts at different temperature (1100-1300℃) and 375 ppm initial S. Influences of various initial S (250-500 ppm) abundances on the trends of Cu was shown in (**d**). The depletion degree of mantle and initial Cu abundance can also change the behavior of Cu (**e**). (**f**) Cu content of silicate melt versus different f_{O_2} (ΔFMQ+1.0, +1.3, +1.6, +2.0) for flux-melting. In (**a-f**), the solid lines represent the melting model induced by slab aqueous fluid, and the dash lines correspond to the slab hydrous melt.

Fig. 8. Variations of $D_{Cu}^{sul/melt}$ along with increasing melting for (**a**) polybaric continuous melting of DMM at different T_p (1300-1400°C), (**b**) isobaric melting of T-SCLMs at various pressure (1.5, 2.7 and 3.9 GPa), (**c**) flux-melting of mantle wedge under distinct temperature (1100, 1150, 1200, 1250 and 1300℃). The red dashed line in (**a**) represent the changes of $D_{Cu}^{sul/melt}$ in the adiabatic decompression melting of PM at 1500℃ T_p. Moreover, the critical values of $D_{Cu}^{sul/melt}$ for the transfer of Cu behavior from downtrend to uptrend are shown as grey dashed lines in (**a**) decompression melting (~360) and (**b**) isobaric melting (~150).

Fig. 9. Island-averaged Ni concentrations corrected for fractionation effect to $Mg^{\#}=0.72$ plotted as a function of the lithosphere thickness. Each data point represents average contents for a given volcanic island; error bars represent standard deviations from the mean. The data are corrected using liquid lines of descent (LLDs) derived from MORB (in Supplementary 6).

Fig. 10. (**a**). MgO wt. % vs. Ni contents of rocks from the oceanic plateaus. (**b**). Inferred temperatures and pressures at which partial melting terminated (in text) for the high-Mg rocks from oceanic plateaus. Diameters of circles in (b) are proportional to the Ni concentrations in samples. The grey area is nominally below the peridotite solidus, which is not perfectly constrained; dashed lines are melting paths. The points farthest to the left of the solidus represent the products of the highest degrees of partial melting. The highest Ni contents are typically found in magmas with the highest pressures and temperatures of equilibration at near-solidus conditions, not the highest aggregate degrees of melting.

Fig. 11. Mantle potential temperatures inferred for rocks from some oceanic and continental LIPs. Oceanic plateaus: Wrangellia, Kerguelen, Ontong Java and Caribbean. Continental LIPs: Deccan, Parana, Siberian Trap, Karoo and Emeishan.

Table 1. Compositions of different sources and fluids used in this work

	SiO_2	Al_2O_3	FeO[a]	MnO	MgO	CaO	Na_2O	K_2O	Cr_2O_5	TiO_2	NiO	CoO	P_2O_5	H_2O	Total	Ni(ppm)	Cu(ppm)	S(ppm)
PM[b]	45	4.45	8.43	0.135	37.8	3.55	0.36	0.029	0.384	0.2	0.25	0.013	0.021	-	100.622	1960	24	250
DMM[c]	44.71	3.98	8.18	0.13	38.73	3.17	0.13	0.006	0.57	0.13	0.24	-	0.019	-	100	1886	24	200
A-SCLM[d]	42.9	0.3	6.5	0.15	49.2	0.1	0.1	-	0.4	0.01	0.30	-	-	-	99.96	2357	1.8	20
P-SCLM[d]	44.6	1.9	7.9	0.12	42.6	1.7	0.12	-	0.4	0.07	0.28	-	-	-	99.69	2200	11.5	112
T-SCLM[d]	44.5	3.5	8.0	0.13	39.8	3.1	0.24	-	0.4	0.14	0.26	-	-	-	100.07	2043	21.1	190
Aqueous fluid[e]	5.52	0.7	0.23	-	0.24	0.13	1	0.12	-	0.03	-	-	-	92	100	-	-	
Hydrous melt[e]	59.02	11.03	0.7	-	0.34	1.14	4.77	2.63	-	0.25	-	-	-	20	99.88	-	-	
Supercritical liquid[f]	29.8	2.89	1.12	-	0.85	3.25	2.64	-	-	0.71	-	-	-	57.6	98.86	-	-	

[a] total Fe as FeO

[b] primitive mantle from McDonough and Sun (1995)

[c] depleted MORB mantle (DMM) from Workman and Hart (2005)

[d] A-SCLM, P-SCLM and T-SCLM from Griffin et al. (2009)

[e] typical aqueous fluid and hydrous melt from Hermann and Spandler (2008)

[f] typical supercritical liquid from Kessel et al. (2005b)

Figure 1.

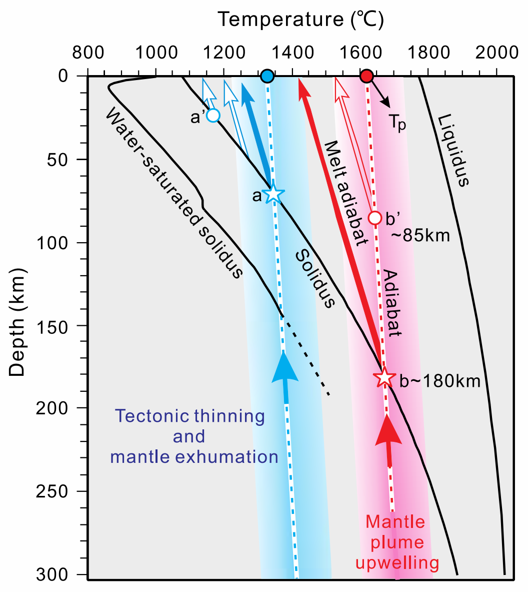
Temperature (℃)
800
1000
1200
1400
1600
1800
2000
0
50
100
150
200
250
300
Depth (km)
Tp
a'
a
Water-saturated solidus
Solidus
Melt adiabat
Adiabat
Liquidus
b'
~85km
b~180km
Tectonic thinning
and
mantle exhumation
Mantle
plume
upwelling

Figure 2.

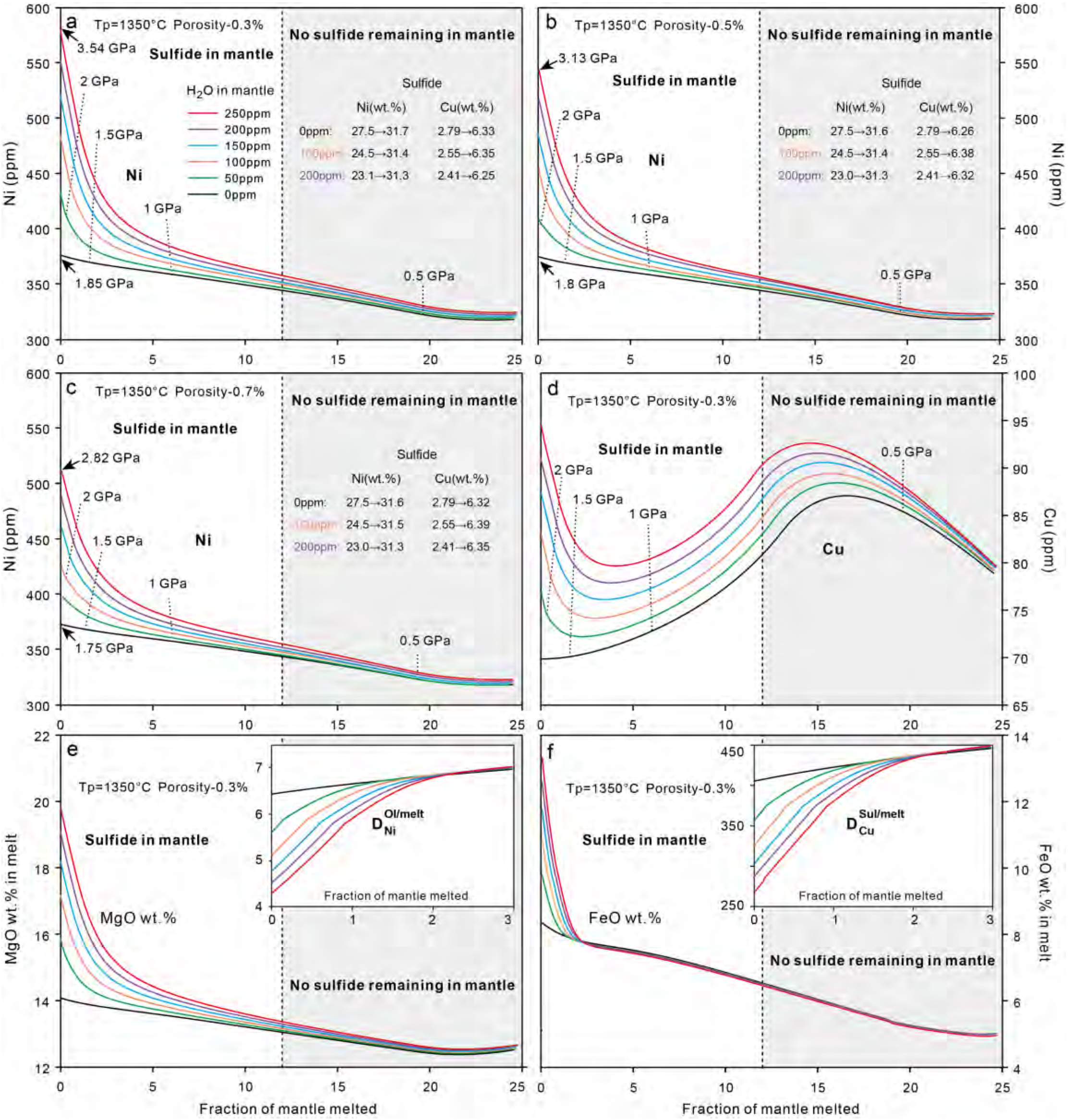
a
Tp=1350°C Porosity-0.3%
3.54 GPa
Sulfide in mantle
2 GPa
1.5GPa
H2O in mantle
250ppm
200ppm
150ppm
100ppm
50ppm
0ppm
Ni
1 GPa
1.85 GPa
No sulfide remaining in mantle
Sulfide
Ni(wt.%) Cu(wt.%)
0ppm: 27.5→31.7 2.79→6.33
100ppm: 24.5→31.4 2.55→6.35
200ppm: 23.1→31.3 2.41→6.25
0.5 GPa
Ni (ppm)
b
Tp=1350°C Porosity-0.5%
3.13 GPa
Sulfide in mantle
2 GPa
1.5 GPa
Ni
1 GPa
1.8 GPa
No sulfide remaining in mantle
Sulfide
Ni(wt.%) Cu(wt.%)
0ppm: 27.5→31.6 2.79→6.26
100ppm: 24.5→31.4 2.55→6.38
200ppm: 23.0→31.3 2.41→6.32
0.5 GPa
Ni (ppm)
c
Tp=1350°C Porosity-0.7%
Sulfide in mantle
2.82 GPa
2 GPa
1.5 GPa
Ni
1 GPa
1.75 GPa
No sulfide remaining in mantle
Sulfide
Ni(wt.%) Cu(wt.%)
0ppm: 27.5→31.6 2.79→6.32
100ppm: 24.5→31.5 2.55→6.39
200ppm: 23.0→31.3 2.41→6.35
0.5 GPa
Ni (ppm)
d
Tp=1350°C Porosity-0.3%
Sulfide in mantle
2 GPa
1.5 GPa
1 GPa
No sulfide remaining in mantle
0.5 GPa
Cu
Cu (ppm)
e
Tp=1350°C Porosity-0.3%
Sulfide in mantle
MgO wt.%
D Ol/melt Ni
Fraction of mantle melted
No sulfide remaining in mantle
MgO wt.% in melt
f
Tp=1350°C Porosity-0.3%
Sulfide in mantle
FeO wt.%
D Sul/melt Cu
Fraction of mantle melted
No sulfide remaining in mantle
FeO wt.% in melt
Fraction of mantle melted
Fraction of mantle melted

Figure 3

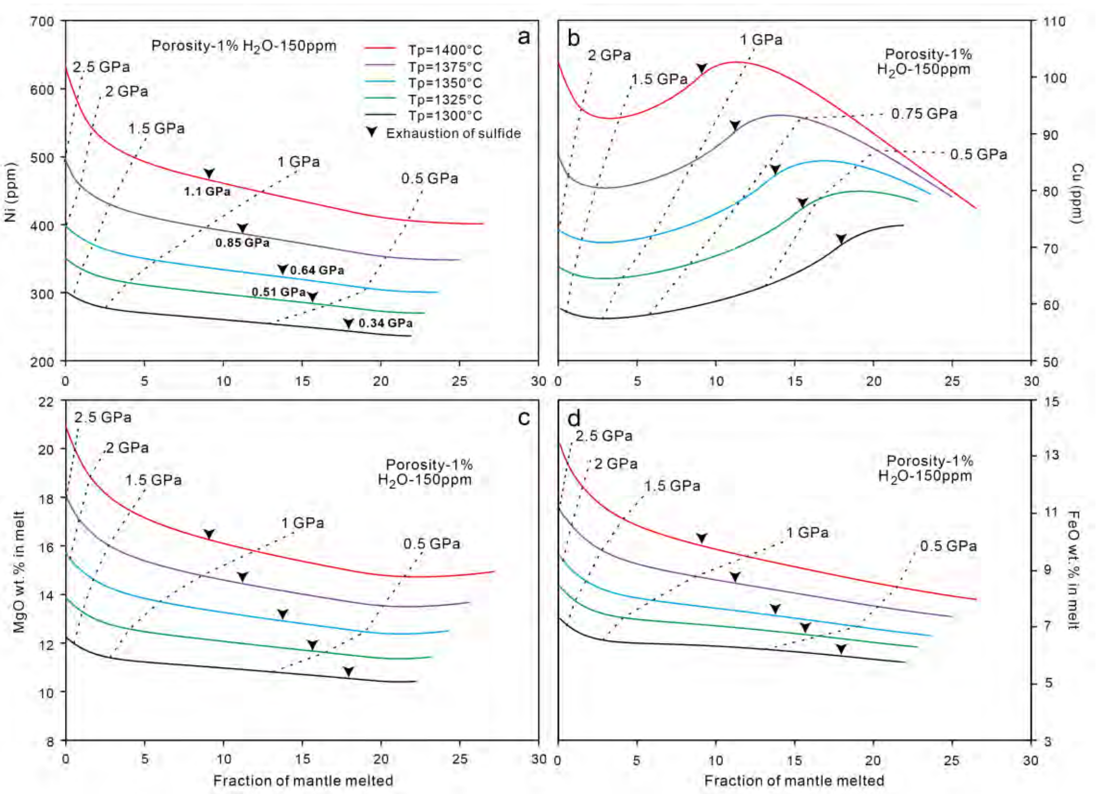
a
Porosity-1% H_2O-150ppm
Tp=1400°C
Tp=1375°C
Tp=1350°C
Tp=1325°C
Tp=1300°C
Exhaustion of sulfide
2.5 GPa
2 GPa
1.5 GPa
1 GPa
0.5 GPa
1.1 GPa
0.85 GPa
0.64 GPa
0.51 GPa
0.34 GPa
Ni (ppm)
700
600
500
400
300
200
b
Porosity-1% H_2O-150ppm
2 GPa
1.5 GPa
1 GPa
0.75 GPa
0.5 GPa
Cu (ppm)
110
100
90
80
70
60
50
c
Porosity-1% H_2O-150ppm
2.5 GPa
2 GPa
1.5 GPa
1 GPa
0.5 GPa
MgO wt.% in melt
22
20
18
16
14
12
10
8
d
Porosity-1% H_2O-150ppm
2.5 GPa
2 GPa
1.5 GPa
1 GPa
0.5 GPa
FeO wt.% in melt
15
13
11
9
7
5
3
0
5
10
15
20
25
30
Fraction of mantle melted
Fraction of mantle melted

Figure 4.

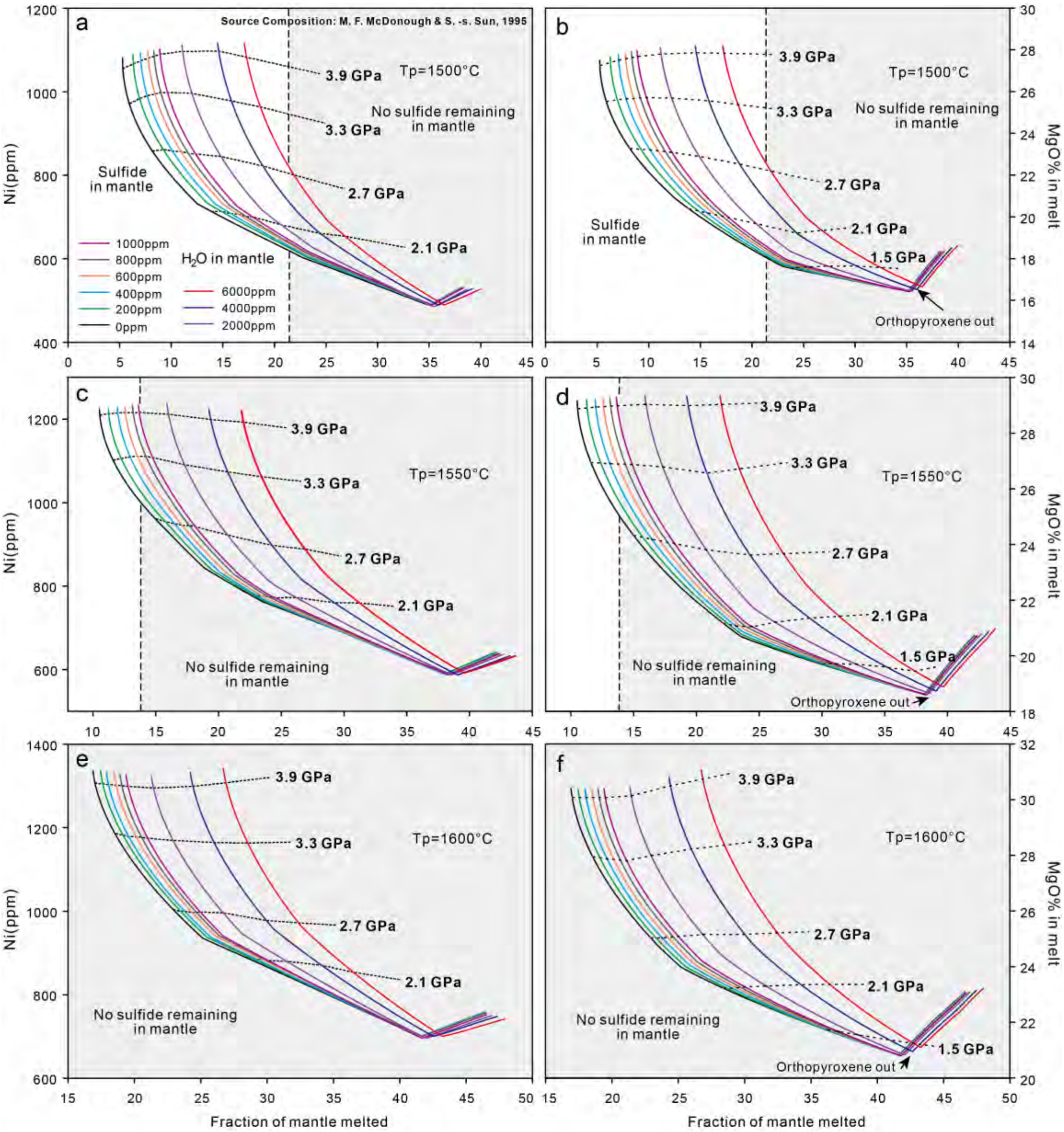

Figure 5.

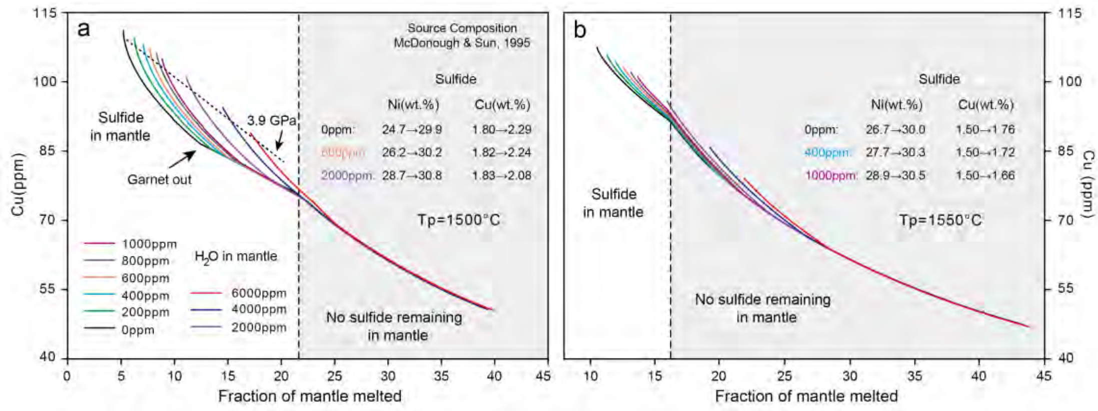

Figure 6.

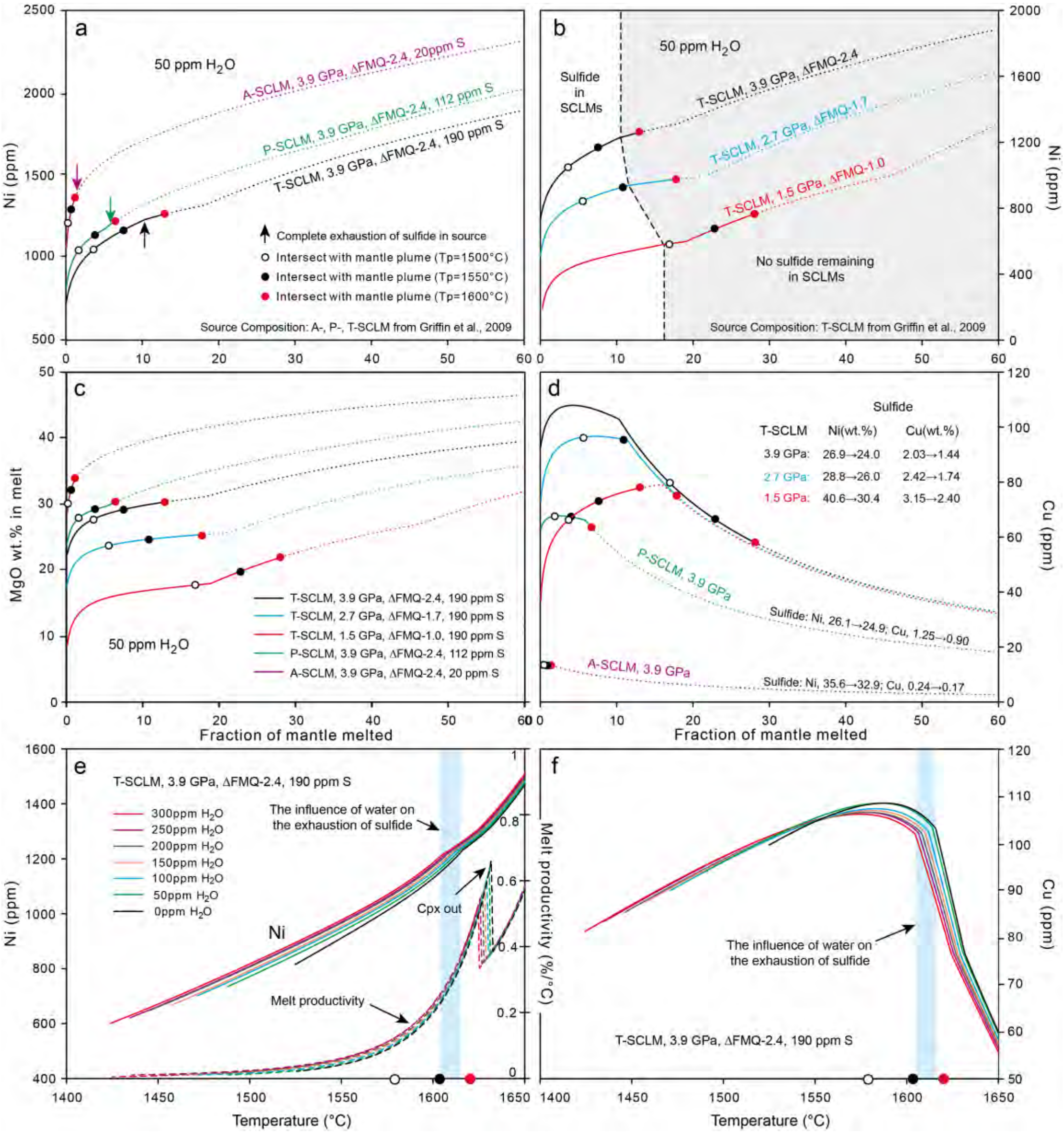
a
50 ppm H_2O
A-SCLM, 3.9 GPa, ΔFMQ-2.4, 20ppm S
P-SCLM, 3.9 GPa, ΔFMQ-2.4, 112 ppm S
T-SCLM, 3.9 GPa, ΔFMQ-2.4, 190 ppm S
Complete exhaustion of sulfide in source
Intersect with mantle plume (Tp=1500°C)
Intersect with mantle plume (Tp=1550°C)
Intersect with mantle plume (Tp=1600°C)
Source Composition: A-, P-, T-SCLM from Griffin et al., 2009
Ni (ppm)
2500
2000
1500
1000
500
0
10
20
30
40
50
60
b
Sulfide in SCLMs
50 ppm H_2O
T-SCLM, 3.9 GPa, ΔFMQ-2.4
T-SCLM, 2.7 GPa, ΔFMQ-1.7
T-SCLM, 1.5 GPa, ΔFMQ-1.0
No sulfide remaining in SCLMs
Source Composition: T-SCLM from Griffin et al., 2009
Ni (ppm)
2000
1600
1200
800
400
0
c
MgO wt.% in melt
50
40
30
20
10
0
50 ppm H_2O
T-SCLM, 3.9 GPa, ΔFMQ-2.4, 190 ppm S
T-SCLM, 2.7 GPa, ΔFMQ-1.7, 190 ppm S
T-SCLM, 1.5 GPa, ΔFMQ-1.0, 190 ppm S
P-SCLM, 3.9 GPa, ΔFMQ-2.4, 112 ppm S
A-SCLM, 3.9 GPa, ΔFMQ-2.4, 20 ppm S
Fraction of mantle melted
d
Sulfide
T-SCLM
Ni(wt.%)
Cu(wt.%)
3.9 GPa: 26.9→24.0 2.03→1.44
2.7 GPa: 28.8→26.0 2.42→1.74
1.5 GPa: 40.6→30.4 3.15→2.40
P-SCLM, 3.9 GPa
Sulfide: Ni, 26.1→24.9; Cu, 1.25→0.90
A-SCLM, 3.9 GPa
Sulfide: Ni, 35.6→32.9; Cu, 0.24→0.17
Cu (ppm)
120
100
80
60
40
20
0
Fraction of mantle melted
e
T-SCLM, 3.9 GPa, ΔFMQ-2.4, 190 ppm S
300ppm H_2O
250ppm H_2O
200ppm H_2O
150ppm H_2O
100ppm H_2O
50ppm H_2O
0ppm H_2O
The influence of water on the exhaustion of sulfide
Cpx out
Ni
Melt productivity
Ni (ppm)
1600
1400
1200
1000
800
600
400
Melt productivity (%/°C)
1
0.8
0.6
0.4
0.2
0
Temperature (°C)
1400
1450
1500
1550
1600
1650
f
The influence of water on the exhaustion of sulfide
T-SCLM, 3.9 GPa, ΔFMQ-2.4, 190 ppm S
Cu (ppm)
120
110
100
90
80
70
60
50
Temperature (°C)

Figure 7.

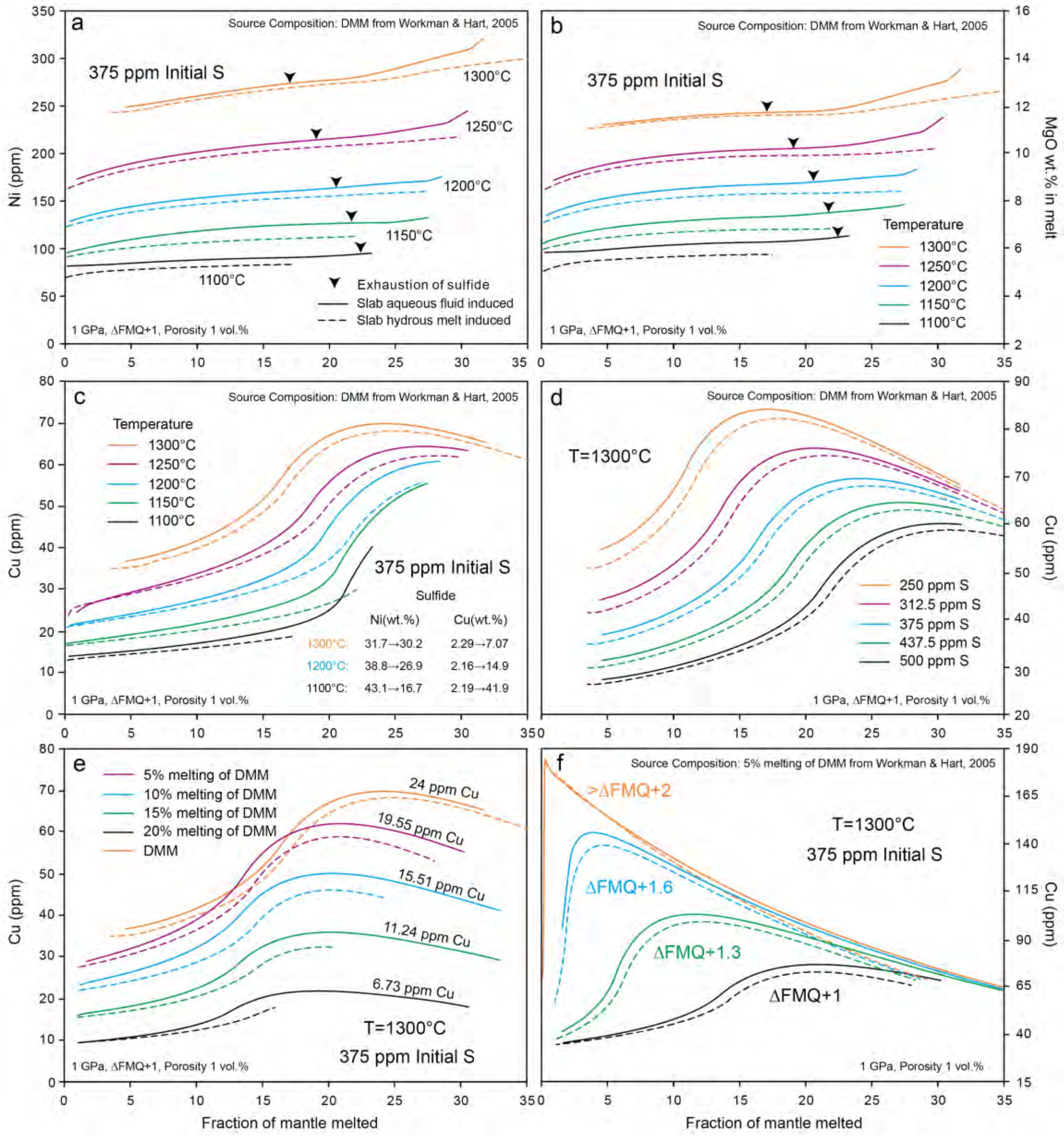
a
Source Composition: DMM from Workman & Hart, 2005
375 ppm Initial S
1300°C
1250°C
1200°C
1150°C
1100°C
Exhaustion of sulfide
Slab aqueous fluid induced
Slab hydrous melt induced
1 GPa, ΔFMQ+1, Porosity 1 vol.%
Ni (ppm)
b
Source Composition: DMM from Workman & Hart, 2005
375 ppm Initial S
Temperature
1300°C
1250°C
1200°C
1150°C
1100°C
1 GPa, ΔFMQ+1, Porosity 1 vol.%
MgO wt.% in melt
c
Source Composition: DMM from Workman & Hart, 2005
Temperature
1300°C
1250°C
1200°C
1150°C
1100°C
375 ppm Initial S
Sulfide
Ni(wt.%)
Cu(wt.%)
1300°C: 31.7→30.2 2.29→7.07
1200°C: 38.8→26.9 2.16→14.9
1100°C: 43.1→16.7 2.19→41.9
1 GPa, ΔFMQ+1, Porosity 1 vol.%
Cu (ppm)
d
Source Composition: DMM from Workman & Hart, 2005
T=1300°C
250 ppm S
312.5 ppm S
375 ppm S
437.5 ppm S
500 ppm S
1 GPa, ΔFMQ+1, Porosity 1 vol.%
Cu (ppm)
e
5% melting of DMM
10% melting of DMM
15% melting of DMM
20% melting of DMM
DMM
24 ppm Cu
19.55 ppm Cu
15.51 ppm Cu
11.24 ppm Cu
6.73 ppm Cu
T=1300°C
375 ppm Initial S
1 GPa, ΔFMQ+1, Porosity 1 vol.%
Cu (ppm)
Fraction of mantle melted
f
Source Composition: 5% melting of DMM from Workman & Hart, 2005
>ΔFMQ+2
T=1300°C
375 ppm Initial S
ΔFMQ+1.6
ΔFMQ+1.3
ΔFMQ+1
1 GPa, Porosity 1 vol.%
Cu (ppm)
Fraction of mantle melted

Figure 8.

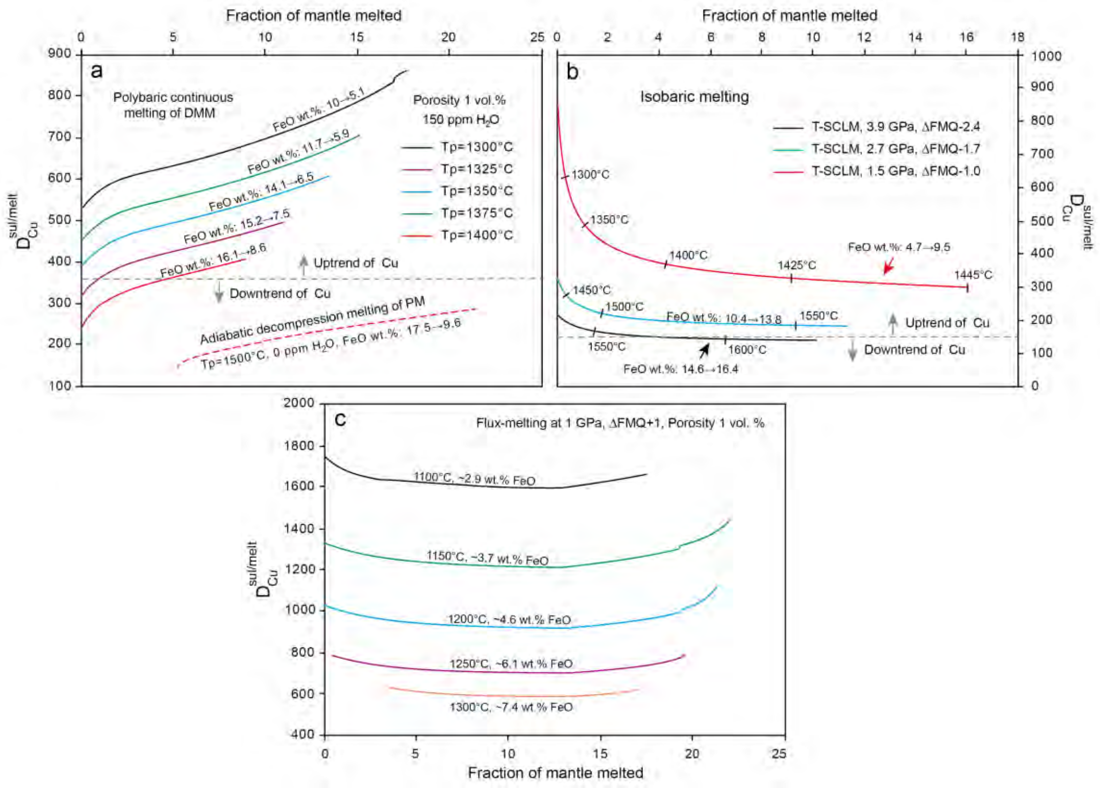

Figure 9.

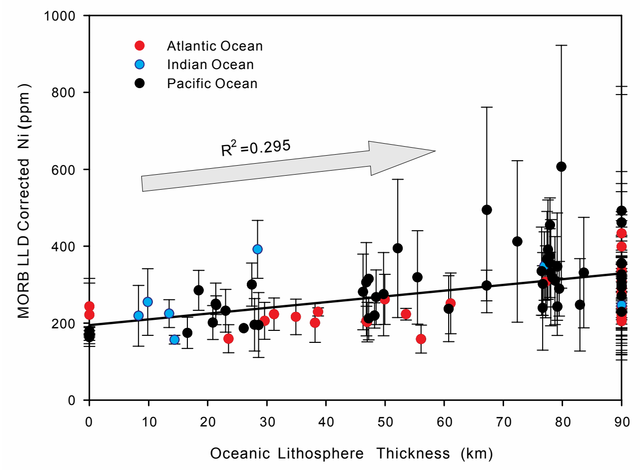

Figure 10.

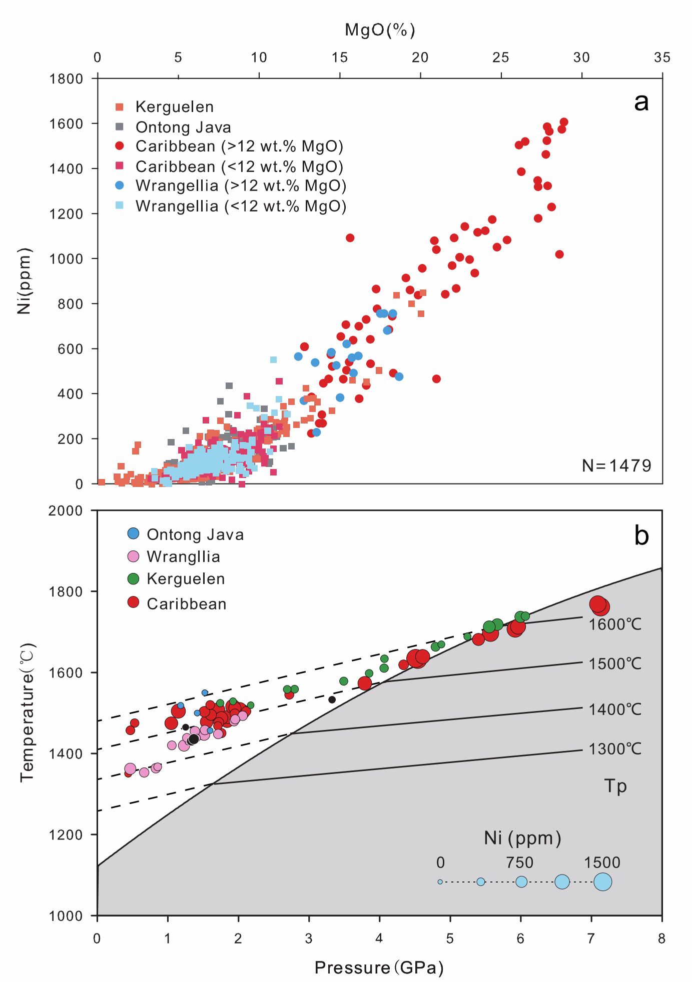

Figure 11.